

THE FORMATION AND EVOLUTION OF SPHERICAL TRAPPING HORIZONS

by

© Lionel Brits

A thesis submitted
in partial fulfillment of the
requirements for the degree of
Bachelors of Science (Honours) in Physics.

Department of Physics and Physical Oceanography
Memorial University of Newfoundland

May 11, 2005

ST. JOHN'S

NEWFOUNDLAND

Abstract

The dynamics of spherically symmetric black holes formed from dust-filled spacetimes are studied in the context of Hayward's trapping horizons – 3-surfaces foliated by marginal 2-surfaces. The relativistic hydrodynamic treatment of Misner and Sharp [1964] is used in the LeMaître-Tolman-Bondi spacetime [Gonçalves, 2001] to model the gravitational collapse of pressure-free dust with various initial density and velocity distributions. Trapping horizons are located in these spacetimes and their signatures examined.

To my parents, Charles and Linda.

Acknowledgements

I would like to thank Dr. Booth for his enthusiastic guidance and supervision. I would also like to thank Kelley for her understanding and companionship, and for keeping me well supplied with sushi.

Table of Contents

1	Introduction	1
1.1	Motivation	1
1.2	Outline	2
2	Theory	4
2.1	Background	4
2.1.1	Coordinate Systems	4
2.1.2	Conformal Compactification	6
2.1.3	Event Horizons	9
2.1.4	Trapping Horizons	12
2.2	Gravitational Collapse	20
2.2.1	Adiabatical Spherical Collapse	20
2.2.2	Pressure-Free Dust	23
2.2.3	Locating the Trapping Horizon	25
2.2.4	Initial Conditions	26
3	Analytical Treatment	29
3.1	Collapse From Rest	29
3.1.1	Inhomogeneous Collapse	29
3.1.2	Oppenheimer-Snyder Collapse	32
3.2	General Inhomogeneous Collapse	33
3.3	Classification	34
4	Results	36
4.1	Oppenheimer-Snyder Collapse	36
4.2	Inhomogeneous Collapse from Rest	37
4.2.1	Single Pulse Falling into a Black Hole	37

4.2.2	Concentric Infalling Shells	46
4.3	Homogeneous Collapse with Initial Velocity	54
4.4	General Inhomogeneous Collapse	57
4.5	Causal Structure	59
4.6	Horizon Signature	60
5	Conclusion	62
5.1	Future Work	63
	Appendices	64
A	Detailed Derivations	64
A.1	Derivation of $\frac{1}{\sqrt{h}}\mathcal{L}_{(\ell)}\sqrt{h} = \theta_{(\ell)}$	64
A.2	Proof that $\tilde{B}_\alpha^\alpha = B_\alpha^\alpha$	66
A.3	Derivation of Equation of Motion	66

List of Figures

2.1	Carter-Penrose diagram	8
2.2	Carter-Penrose diagram of a black hole (schematic)	10
2.3	Foliation of Trapping Horizon by Marginal Surfaces	13
4.1	Oppenheimer-Snyder Collapse	38
4.2	Density profile: single pulse	39
4.3	Gravitational collapse and trapping horizon: single pulse	41
4.4	Trapping horizon signature: single pulse	41
4.5	Density profile: single denser pulse	42
4.6	Gravitational collapse and trapping horizon: single denser pulse	43
4.7	Trapping horizon signature: single denser pulse	44
4.8	Density profiles: single pulses with varying densities	45
4.9	Gravitational collapse and trapping horizons: single pulses with varying densities	46
4.10	Density profile: multiple infalling shells, case 1	47
4.11	Gravitational collapse and trapping horizon: multiple infalling shells, case 1	48
4.12	Trapping horizon signature: multiple infalling shells, case 1	49
4.13	Density profile: multiple infalling shells, case 2	50
4.14	Gravitational collapse and trapping horizon: multiple infalling shells, case 2	51
4.15	Trapping horizon signature: multiple infalling shells, case 2	51
4.16	Density profile: two concentric pulses	52
4.17	Gravitational collapse and trapping horizon: two concentric pulses	53
4.18	Trapping horizon signature: two concentric pulses	54
4.19	Time-to-collapse: uniform density with initial velocity	55

4.20	Gravitational collapse and trapping horizon: uniform density with initial velocity	56
4.21	Trapping horizon signature: uniform density with initial velocity . . .	56
4.22	Density profile: multiple infalling shells, case 3	57
4.23	Gravitational collapse and trapping horizon: multiple infalling shells, case 3	58
4.24	Trapping horizon signature: multiple infalling shells, case 3	58
4.25	Observer leaving and reentering trapped region	60

Chapter 1

Introduction

1.1 Motivation

The unification of quantum mechanics, a theory which describes the interaction of matter on a small scale, with relativity, which describes the large scale structure of space and time, has been a pressing goal in theoretical physics since the inception of these disparate theories. Two contending theories that bridge this gap are loop quantum gravity and string theory, both promising, yet still in their infancy. A hint that a deeper, fundamental link between relativity and quantum theory exists may lie in the study of black holes. Much work in the last three decades has resulted from the formulation of four laws of black hole mechanics by Bardeen, Carter, and Hawking [Bardeen et al., 1973]. These laws mathematically reflect the laws of thermodynamics, suggesting an inherent statistical description embedded within relativity theory.

The study of black hole dynamics has also provided a driving force for numerical relativity, especially in the study of gravitational waves [Kimberly, 2003] and critical phenomena [Gundlach, 1999, Choptuik, 1994]. Black holes are also an important source of new developments in relativistic astrophysics, and are good candidates for

sources of gravitational waves, which, if detected by observatories such as LIGO and VIRGO, would provide new methods for testing the theory of relativity as well as many astrophysical and cosmological models [Kimberly, 2003].

There are still many open questions in general relativity, such as the principle of cosmic censorship, and the quantum mechanical nature of black holes. When studying the dynamic behaviour of these objects, a difficulty arises in that the boundaries, or event horizons, that define them cannot be pinpointed locally, but instead can only be located after knowing the entire futures of the systems being studied. Thus the conventional definition of black holes is unsuitable for modelling and numerical simulation, and this has led to the formulation of a number of alternate definitions of black holes solely in terms of local measurements. One such construct is the future outer trapping horizon, as described by Hayward [1994]. Though these definitions lend themselves to practical study, especially in numerical work, several questions regarding the theory still remain, including whether these boundaries are always mathematically well-behaved and physically realistic. Exact solutions are known only for a restricted set of space-times, including Oppenheimer-Snyder homogeneous-isotropic collapse, and the Vaidya space-time, which describes a space-time with a null fluid as the gravitational source [Ashtekar and Krishnan, 2003]. While these solutions are certainly tractable, there is a definite need to study these horizons in more general settings.

1.2 Outline

The focus of this work is the study of the evolution of a restricted class of black holes, namely spherically symmetric, collapsing, pressure-free distributions of matter, in the context of trapping horizons – 3-surfaces on which the expansion of outgoing

null rays is momentarily halted. The mathematical treatment that describes the collapse follows that of Wheeler et al. [1973], and solutions to the LeMaître-Tolman-Bondi spacetime [Gonçalves, 2001] are used to obtain the defining equations for the trapping horizons.

Trapped regions are located and studied analytically in the well-known Oppenheimer Snyder solution as well as inhomogeneous matter distributions. Various density and velocity profiles are used to locate and investigate the nature of these trapping horizons, in particular their signatures and causal properties.

Chapter 2

Theory

2.1 Background

2.1.1 Coordinate Systems

Coordinate Singularities

Although it is inviting to consider the behaviour of moving bodies with respect to some reasonably stable reference frame, i.e., one that is far removed from any gravitational effects and can be considered to be “at rest”, the very nature of GR allows for situations in which separate observers may have irreconcilably different viewpoints of the same event.

The simplest example is possibly the Schwarzschild solution to the field equations, which describes the vacuum space-time surrounding a massive, spherically symmetric object. If the object is sufficiently concentrated, so that it lies entirely within its Schwarzschild radius $R_S = 2M$, then R_S defines an imaginary boundary from which no object or signal can ever escape. From the viewpoint of a distant observer, an observer moving towards the object will seem to approach the radius R asymptotically,

never in fact reaching it. If the distant observer were to describe the spacetime by the time t as measured in his frame, and by the proper circumferential coordinate $r = \frac{C}{2\pi}$, then he will find the metric to be singular at R_S . Additionally, inside the Schwarzschild radius he will find that the time coordinate t has become spacelike, and similarly the radial coordinate r has become timelike.

On the other hand, the situation is very different for the observer approaching the Schwarzschild radius. She will notice nothing peculiar about this radius as she passes beyond it, and will even find the metric to be regular everywhere except at $r = 0$. However, the extreme curvature of gravity has now distorted her future-directed light-cone so that all signals emitted by her reach the singularity that has formed at $r = 0$ within a finite lapse of proper time. She is therefore also destined to fall into the singularity within this time.

The disagreement between the two observers arises because while the distant observer makes his measurements relative to a stationary reference frame, there can be no stationary frames inside the Schwarzschild radius R_S , and so the viewpoint of one observer takes on a different meaning in the reference frame of the other. The singularity at $r = 2M$ as determined by the distant observer is called a *coordinate singularity*, to distinguish it from the true singularity that exists at $r = 0$, where the curvature becomes infinite. The singularity at $r = 2M$ can be eliminated by transforming r and t into another suitable set of coordinates, such as the position r and proper time τ of the infalling observer. The true singularity at $r = 0$ however cannot be removed.

Co-moving Coordinates

It is often useful to transform one's coordinate system into another coordinate system attached to some family of infalling time-like or null curves; these are so-called *co-*

moving coordinates. Examples of such coordinate systems include Kruskal-Szekeres coordinates, Eddington-Finkelstein coordinates, which are attached to ingoing radial null geodesics, and generalized Painlevé-Gullstrand coordinates, which are attached to timelike observers falling radially inward from infinity [Martel and Poisson, 2001].

2.1.2 Conformal Compactification

In order to properly analyze the geometry of space-time, in particular its causal structure, we need to consider so-called “points at infinity”. One convenient tool for analyzing this region of space-time is the *Carter-Penrose diagram*, in which points at infinity are brought in to finite distances by a process called *conformal compactification* [Townsend, 1997]. A conformally compactified spacetime is obtained by a *conformal mapping* which defines a new metric by multiplying the original, physical metric by some scalar field, i.e.

$$\bar{g}_{\alpha\beta} = \Omega^2 g_{\alpha\beta}. \tag{2.1}$$

We can create a Carter-Penrose diagram for the Minkowski spacetime by first introducing the null coordinates $u = t + r$ and $v = t - r$, which may be thought of as left- and right-moving light rays in the spacetime. The metric in spherical coordinates is then

$$ds^2 = -dudv + \frac{1}{4}(u - v)^2(d\Omega^2), \tag{2.2}$$

where $d\Omega^2$ is the metric on the 2-sphere, not to be confused with the conformal factor Ω^2 . Making the substitution $U = \arctan u$ and $V = \arctan v$, we see that we’ve mapped the domain $(-\infty, \infty)$ onto $(-\frac{\pi}{2}, \frac{\pi}{2})$, thus compactifying the space-time. The

new metric is then

$$d\tilde{s}^2 = \sec^2 U \sec^2 V \left[dU dV + \frac{1}{4} \sin^2(U - V)(d\Omega^2) \right]. \quad (2.3)$$

We can transform U and V back into time-like and radial space-like coordinates: $\tilde{t} = U + V$ and $\tilde{r} = U - V$. The new metric is then,

$$d\tilde{s}^2 = \frac{1}{4} \sec^2 U \sec^2 V \left[-d\tilde{t}^2 + d\tilde{r}^2 + \sin^2(\tilde{r})(d\Omega^2) \right]. \quad (2.4)$$

The space-time parameterized in terms of these new coordinates is shown in Figure 2.1. In the way the Carter-Penrose diagram is normally presented, each point represents a particular 2-sphere, so that two angular degrees of freedom are suppressed. One may imagine rotating the diagram around its vertical axis, in which case one angular degree of freedom may be recovered.

Causal Structure

Some important features of the Carter-Penrose diagram are to be noted. Firstly, since the mapping that produced the diagram is conformal, i.e. angle-preserving, in-going and out-going light-rays remain at 90° to one another. The boundary of the diagram does not actually belong to the original space-time, and is called *conformal infinity*. The boundary can be subdivided into 4 regions as shown in the diagram. The points i^+ , i^0 and i^- are known as *future timelike-*, *spatial-*, and *past timelike infinity* respectively. All timelike geodesics originate at i^- and terminate at i^+ , while spacelike geodesics both originate and terminate at i^0 . Therefore i^+ and i^- can be thought of the infinite future and infinite past of some timelike observer moving along a geodesic.

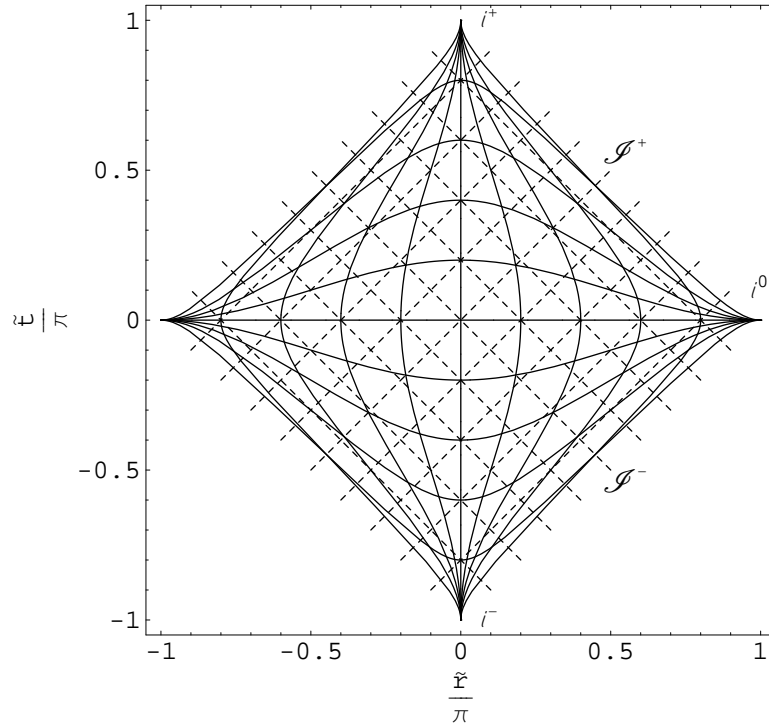


Figure 2.1: The Minkowski space-time conformally compactified and presented as a Carter-Penrose diagram. Here $\tilde{t} = \arctan(r + t) - \arctan(r - t)$ while $\tilde{r} = \arctan(r + t) + \arctan(r - t)$. Horizontally directed curves are curves of constant t , while vertically directed curves are curves of constant r . Left and right-moving null geodesics (lightrays) are drawn as dashed lines.

The surfaces \mathcal{I}^+ , and \mathcal{I}^- , pronounced “Scri-Plus” and “Scri-Minus”, are known as *future-* and *past null infinity* respectively. All null geodesics therefore originate on \mathcal{I}^- and terminate at \mathcal{I}^+ .

We can further denote the set $J^-(p)$ of all points on the space-time that can send signals to, i.e. are causally connected to, some particular point p . We call this set the *causal past* of p . Similarly, we can denote $J^+(p)$ of all points on the space-time that can receive signals from p , and we can call this set the *causal future* of p . See Hawking and Ellis [1973] and Townsend [1997] for a comprehensive treatment of the causal structure of spacetime.

2.1.3 Event Horizons

With this conformal structure in place, we can analyze the causal nature of the Schwarzschild space-time. While this is not only instructive, it will prove to be useful since Birkhoff’s Theorem states that the Schwarzschild metric is the unique spherically symmetric solution to the field equations *in vacuo* [Wald, 1984].

Recalling the discussion about the two observers in the Schwarzschild space-time separated by the 2-surface $r = R_S$, we notice that the 3-surface foliated by these 2-surfaces divides the space-time into two regions: points outside the surface, which can send signals to \mathcal{I}^+ , and points inside the surface which cannot. The region outside the 3-surface R_S therefore forms the *causal past of future null infinity*, or $J^-(\mathcal{I}^+)$. Consequently, the region inside the surface is causally disconnected from the outside spacetime in the sense that it does not belong to $J^-(\mathcal{I}^+)$. Given our static Schwarzschild space-time manifold \mathcal{M} , we can say that the region inside the 3-surface R_S is $\mathcal{M} - J^-(\mathcal{I}^+)$. The 3-surface then forms the boundary of $J^-(\mathcal{I}^+)$, which we denote by $\dot{J}^-(\mathcal{I}^+)$

Our prescription that the space-time containing our massive object is static allowed us to identify the 3-surface surface $r = R_S$ with $\dot{J}^-(\mathcal{I}^+)$. In general, our space-time will be dynamic, so that we may not be able to easily determine $\dot{J}^-(\mathcal{I}^+)$, if at all. However these concepts are still useful to us, so that in general we will call $\dot{J}^-(\mathcal{I}^+)$ the *event horizon*, and the region $\mathcal{M} - J^-(\mathcal{I}^+)$ a *black hole*, or the union of all black holes. The causal structure of a space-time containing a single black hole is summarized in Figure 2.2 in schematic form.

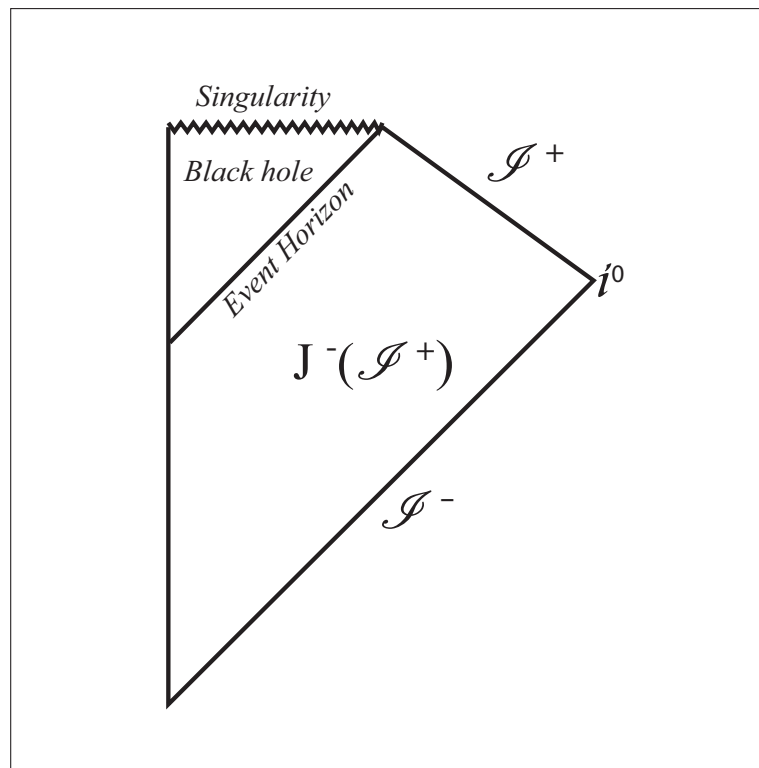


Figure 2.2: The causal structure of a black hole is shown here as a Carter-Penrose diagram, where the event horizon is shown as the boundary of $J^-(\mathcal{I}^+)$. Note that actual dimensions in this diagram are meaningless, as it is only representative of a space-time defined up to a conformal factor. Also, since the mapping is conformal, in-going and out-going light-rays remain at 45° to one another (though they have been omitted for clarity).

While the above definitions are certainly precise, in general they are not very useful. In order to know the extent of $J^-(\mathcal{I}^+)$, we would have to evolve our space-time into infinity to determine which signals reached \mathcal{I}^+ . Clearly this is impossible to do. In fact, event horizons are by their nature very non-local objects. Their location cannot be determined by purely local measurements, or by local knowledge of the metric.

To illustrate this difficulty, consider a spherically symmetric shell of matter converging towards our location from a great distance. If the shell is massive enough, so that at some later point in time it will be contained entirely within its Schwarzschild radius $R_S = 2M$, then an event horizon, and consequently a black hole will be formed. (Contrast this with our Sun, for which $R_S \ll R_\odot$, where a black hole does not form because the entire mass is not concentrated within its Schwarzschild radius.) We see that if we are presently inside R_S , then in order to escape the black hole, we must reach R_S before the shell of matter does. Then, if we are to wait until the very last possible moment, our future-directed light cone that intersects $r = R_S$, coincident with the shell of matter will form the beginning of the event horizon. From that point forward $r = R_S$ will constitute the remainder of the horizon. Any points both inside the light-cone and $r = R_S$ will not be able to escape the black hole and will become trapped.

Since the shell was spherically symmetric to begin with, it will not emit radiation of any sort, so that its presence will not be known to us through any local measurements. Then, if the space-time did not evolve any further after the shell reached $r = R_S$, observers outside this surface would be justified in identifying it as the event horizon. Otherwise, they too would have no way of detecting any further infalling shells of matter, so that in effect only hypothetical observers at \mathcal{I}^+ would have the advantage of being able to pinpoint the event horizon. Clearly, while helpful in defining exactly

what a black hole is mathematically, the concept of an event horizon is of little practical use in locating a black hole. In addition, it should be noted that an event horizon is only defined in an asymptotically flat spacetime, which further restricts the definition's usefulness [Hawking and Ellis, 1973]. We therefore need to find a suitable alternative that can be defined in terms of local properties of space-time.

2.1.4 Trapping Horizons

One particular boundary that captures the idea of a black hole and that can be defined locally is the so-called *Trapping Horizon* [Hayward, 1994], defined as the boundary of a space-time region in which initially divergent light rays eventually converge. This boundary can be located by investigating the behaviour of light cones in the region.

Consider a sufficiently massive point gravitational source around which an imaginary spherical shell is constructed. If at some time a light signal is emitted radially outward from the sphere, whilst another is simultaneously emitted radially inward from the same point, then the evolution of these two signals will depend on both the strength of the gravitational source and their proximity to it. If the signals are emitted sufficiently far away from the source, the outwardly directed signal will initially move outwardly away from the gravitational source, while the inwardly directed signal will move towards the source, consistent with our everyday expectations. However, if the signals are emitted sufficiently close to the source, both the out- and inwardly directed signals will initially fall inward due to the curvature produced by the source. Any signal emitted from within this region will therefore be trapped inside it, and so we define the sphere or 2-surface from which the signals were emitted as a *trapped surface* enclosing some *trapped region* in space [Penrose, 1964, Wald, 1984].

The boundary of this trapped region is defined by the surface for which the out-

wardly directed signal is initially parallel to the surface itself, so that the signal is momentarily neither escaping nor falling into the surface. Calling this 2-surface a *marginal surface*, we can define the trapping horizon to be the 3-surface generated by the foliation of these marginal surfaces [Hayward, 1994]. A special subset of this definition is the isolated horizon, which is a null 3-surface foliated by marginal surfaces [Ashtekar, 2000]. Note that a marginal surface should not be confused with the concept of a marginally trapped surface, as defined by Hawking and Ellis [1973], where the expansion is only assumed to be non-positive.

The situation given above is illustrated for a hypothetical space-time in Figure 2.3. It is important to note that these definitions make some assumptions about the global geometrical and topological structure of the space-time. In particular, it is assumed that the space-time is asymptotically flat so that the behaviour of "points at infinity" is well defined and regular.

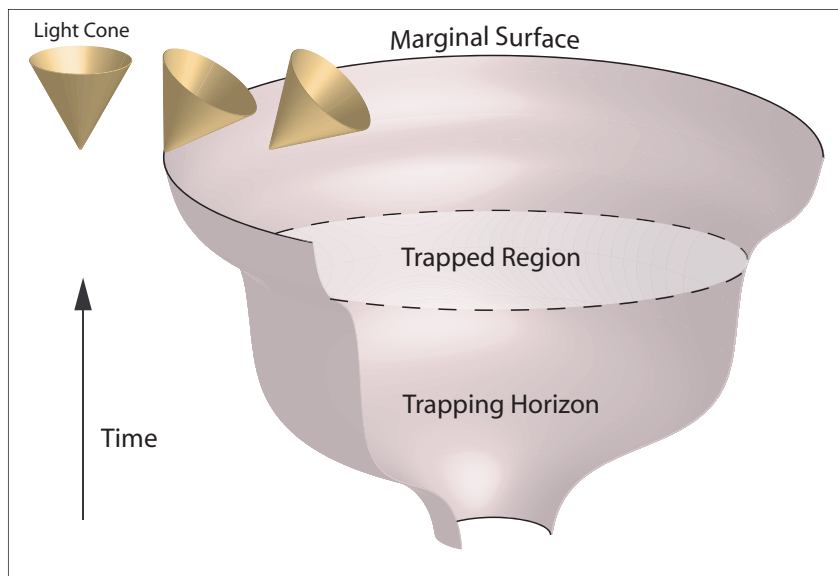


Figure 2.3: A trapping horizon foliated by marginal surfaces is shown here. Inside trapped regions outwardly directed light signals momentarily fall inwards.

The benefit of dealing with trapped surfaces is that we only need to consider the initial behaviour of the emitted signals, without having to mention concepts such as “escape towards infinity” or to consider the final fate of the space-time region, affording us a purely local definition. Although the above discussion dealt with a static, spherically symmetric spacetime, trapped surfaces can be defined more generally and precisely by considering the kinematics of null geodesics.

Congruences of Null Geodesics

A *congruence of curves* in some open set in a manifold \mathcal{M} is a family of curves such that for each point in the set exactly one curve passes through it [Wald, 1984, Townsend, 1997]. We can then specifically consider a *congruence of null geodesics*, where each curve in the family is a null geodesic. These curves are nowhere intersecting so that their tangent vectors ℓ^α define a vector field on the open set. In order to measure the degree to which geodesics are converging or diverging, we look at the evolution of the *deviation vector* ξ^α between two neighbouring geodesics as a function of some affine parameter η . This vector is both orthogonal to, and Lie transported along the geodesics [Poisson, 2004], so that:

$$\ell^\alpha \ell_\alpha = 0, \tag{2.5}$$

$$\ell^\alpha \xi_\alpha = 0, \tag{2.6}$$

$$\ell^\alpha_{;\beta} \ell^\alpha = 0, \text{ and} \tag{2.7}$$

$$\mathcal{L}_\ell \xi^\alpha = 0 \Rightarrow \ell^\alpha_{;\beta} \xi^\beta = \xi^\alpha_{;\beta} \ell^\beta. \tag{2.8}$$

We can introduce the *evolution tensor*

$$B_{\alpha\beta} = \ell_{\alpha;\beta}, \quad (2.9)$$

which measures the failure of ξ^α to be parallel transported along the curve [Poisson, 2004]. Notice that $\frac{D\xi^\alpha}{d\eta} = \xi^\alpha_{;\beta}\ell^\beta = \ell^\alpha_{;\beta}\xi^\beta = B^\alpha_\beta\xi^\beta$. Since we are concerned with the degree to which neighbouring geodesics are diverging we only need to look at the behaviour of ξ^α transverse to the congruence. That is, the behaviour of ξ^α within the surface Σ orthogonal to the congruence. To do so we introduce the *transverse metric* $h_{\alpha\beta}$ given by

$$h_{\alpha\beta} = g_{\alpha\beta} + \ell_\alpha n_\beta + n_\alpha \ell_\beta, \quad (2.10)$$

where n^α is some auxiliary null vector field which does not lie in the congruence, for which we impose $n^\alpha \ell_\alpha = -1$. To see that $h_{\alpha\beta}$ is orthogonal to both ℓ^α and n^α , notice that $h_{\alpha\beta}\ell^\beta = \ell_\alpha - \ell_\alpha + 0 = 0$, and similarly for n^α . Also notice that $h^\alpha_\alpha = 2$ so that Σ is essentially two-dimensional. We can then calculate the transverse component of ξ^α , denoted by $\tilde{\xi}^\alpha$, by projecting it with h^α_β

$$\tilde{\xi}^\alpha = h^\alpha_\beta \xi^\beta. \quad (2.11)$$

The geodesic deviation is now $\tilde{\xi}^\alpha_{;\beta}\ell^\beta = h^\alpha_\mu \xi^\mu_{;\beta}\ell^\beta + h^\alpha_{\mu;\beta}\ell^\beta \xi^\mu$ which can be rewritten as $h^\alpha_\mu B^\mu_\beta \xi^\beta + (n_{\mu;\beta}\xi^\mu \ell^\beta)\ell^\alpha$, where we have made use of the fact that $\ell_\alpha \xi^\alpha = 0$. Since $\tilde{\xi}^\alpha_{;\beta}\ell^\beta$ still has a component parallel to ℓ^α we need to project it with h^α_β again, giving

$$\widetilde{(\tilde{\xi}^\alpha_{;\beta}\ell^\beta)} = h^\alpha_\mu \widetilde{\xi^\mu_{;\beta}\ell^\beta}. \quad (2.12)$$

The Expansion Scalar

We can further rewrite $(\widetilde{\xi^\alpha \ell^\beta})$ as $\tilde{B}_\beta^\alpha \tilde{\xi}^\beta$ where \tilde{B}_β^α is the transverse component of B_β^α and is equal to $h_\mu^\alpha h_\beta^\nu B_\nu^\mu$. Now, we can decompose $\tilde{B}_{\alpha\beta}$ into trace, trace-free symmetric and trace-free antisymmetric parts,

$$\tilde{B}_{\alpha\beta} = \frac{1}{2}\theta h_{\alpha\beta} + \sigma_{\alpha\beta} + \omega_{\alpha\beta}, \quad (2.13)$$

where θ is the *expansion scalar*, given by the trace \tilde{B}_α^α , $\sigma_{\alpha\beta}$ is the *shear tensor* given by $\tilde{B}_{(\alpha\beta)} - \frac{1}{2}\theta h_{\alpha\beta}$, and $\omega_{\alpha\beta}$ is the *rotation tensor* given by $\tilde{B}_{[\alpha\beta]}$. In the case ℓ^α results from an affine parameterization of the congruence, then the following result also holds

$$\tilde{B}_\alpha^\alpha = \ell^\alpha_{;\alpha}, \quad (2.14)$$

See Appendix A.2. The scalar θ is of particular interest since it is a measure of the fractional rate of change of the congruence's cross-sectional area [Poisson, 2004], i.e.

$$\theta = \frac{1}{\delta A} \frac{d}{d\eta} \delta A. \quad (2.15)$$

We can see this by considering the pullback of $h_{\alpha\beta}$ onto Σ , called the *induced metric* on Σ , which we will denote by h_{ij} , where i and j range over 1,2. Then $\varepsilon_{ij} = \sqrt{h}\epsilon_{ij}$ is the area 2-form on Σ , where $h = \det h_{ij}$, so that

$$\begin{aligned}
\frac{d\sqrt{h}}{d\eta} &= \mathcal{L}_\ell \sqrt{h} \\
&= \frac{1}{2\sqrt{h}} \mathcal{L}_\ell h \\
&= \frac{1}{2} \sqrt{h} h^{\alpha\beta} \mathcal{L}_\ell h_{\alpha\beta} \\
&= \sqrt{h} h^{\alpha\beta} \ell_{\beta;\alpha} \\
&= \sqrt{h} \ell^\alpha_{;\alpha} \\
&= \sqrt{h} \theta.
\end{aligned}$$

Therefore we see that θ gives the fractional rate of change of the area element along ℓ^α on Σ . A detailed derivation is given in Appendix A.1.

Raychaudhuri's Equation

In order to determine the evolution of θ along the congruence we must first find the appropriate expression for $\tilde{B}_{\alpha\beta}$, or equivalently that of $B_{\alpha\beta}$ since $\theta = \ell^\alpha_{;\alpha} = B^\alpha_\alpha$ also.

$$\begin{aligned}
B_{\alpha\beta;\gamma} \ell^\gamma &= \ell_{\alpha;\beta\gamma} \ell^\gamma \\
&= -B_{\alpha\gamma} B^\gamma_\beta - R_{\alpha\gamma\beta\delta} \ell^\gamma \ell^\delta.
\end{aligned}$$

(See Appendix A.2 for a detailed derivation.) Taking the trace of $B_{\alpha\beta}$ gives the suitable equation for $\frac{d\theta}{d\eta} = \ell^\alpha_{;\beta} \ell^\beta$.

$$\begin{aligned}
\frac{d\theta}{d\eta} &= -B^{\alpha\gamma} B_{\gamma\alpha} - R_{\alpha\gamma} \ell^\alpha \ell^\gamma \\
&= -\left(\frac{1}{2}\theta^2 + \sigma^{\alpha\beta} \sigma_{\alpha\beta} - \omega^{\alpha\beta} \omega_{\alpha\beta}\right) - R_{\alpha\gamma} \ell^\alpha \ell^\gamma.
\end{aligned}$$

Finally, this gives the *null version of Raychaudhuri's equation* [Wald, 1984, Poisson, 2004]:

$$\frac{d\theta}{d\eta} = -\frac{1}{2}\theta^2 - \sigma^{\alpha\beta}\sigma_{\alpha\beta} + \omega^{\alpha\beta}\omega_{\alpha\beta} - R_{\alpha\gamma}\ell^\alpha\ell^\gamma. \quad (2.16)$$

Note that in order to have $\theta = \ell^\alpha_{;\alpha}$, we have assumed that we are dealing with an affine parameterization of the geodesics, so that $\ell^\alpha_{;\beta}\ell^\beta = 0$. In general, we would need to calculate the trace, $\theta = \tilde{B}^\alpha_\alpha$.

Null Energy Condition

Consider the quantity $R_{\alpha\beta}u^\alpha u^\beta$ where u^α is the 4-velocity of some observer. Using Einstein's equation $R_{\alpha\beta} - \frac{1}{2}Rg_{\alpha\beta} = 8\pi T_{\alpha\beta}$, which we can rewrite as $R_{\alpha\beta} = 8\pi(T_{\alpha\beta} - \frac{1}{2}Tg_{\alpha\beta})$, we can write $R_{\alpha\beta}u^\alpha u^\beta = 8\pi(T_{\alpha\beta}u^\alpha u^\beta + \frac{1}{2}T)$ if u^α is time-like, or $R_{\alpha\beta}u^\alpha u^\beta = 8\pi T_{\alpha\beta}u^\alpha u^\beta$ if u^α is null. The *weak energy condition* states that the energy density measured by an observer whose 4-velocity is u^α is non-negative, which is believed to hold for all classical systems and possibly on average for quantum systems [Wald, 1984]. We therefore have that $T_{\alpha\beta}u^\alpha u^\beta \geq 0$, and by continuity, this will hold if u^α is null. We therefore have the *null energy condition*: For all null ℓ^α ,

$$T_{\alpha\beta}\ell^\alpha\ell^\beta \geq 0. \quad (2.17)$$

Focusing Theorem

If the congruence is *hypersurface orthogonal*, meaning that $\ell_\alpha \propto \Phi_{;\alpha}$ for some scalar field Φ which is constant along the cross section of the congruence, then by Frobenius' theorem, $\omega_{\alpha\beta} = 0$, i.e. the congruence is twist-free. Also, since $\sigma_{\alpha\beta}$ has only a

transverse component, $\sigma^{\alpha\beta}\sigma_{\alpha\beta} \geq 0$. We therefore find, using Eqns. (2.16,2.17), that

$$\frac{d\theta}{d\eta} + \frac{1}{2}\theta^2 \leq 0. \quad (2.18)$$

That is, the second derivative of the congruence's cross-sectional area with respect to η is always negative or zero. If the congruence is initially diverging, so that $\theta_0 > 0$, then the rate of expansion will decrease with increasing η . On the other hand, if the congruence is initially converging, so that $\theta_0 < 0$, then $\theta \rightarrow -\infty$ within a lapse of affine parameter $\Delta\eta \leq \frac{2}{|\theta_0|}$. Points at which this occurs are called *caustics* and arise where null geodesics fail to extremize the proper path length between two conjugate points. See [Wald, 1984] for discussion.

Trapped and Marginal Surfaces

We can now more precisely define a trapped surface as a 2-surface on which the expansion of a congruence of outwardly directed null geodesics is negative or zero. Let ℓ^α be tangent to the congruence, and define the *outward null expansion* to be $\theta_{(\ell)}$. Then a trapped surface is defined by the condition that $\theta_{(\ell)} \leq 0$.

We can also define a marginal surface to be trapped surface on which $\theta_{(\ell)} = 0$, and where $\theta_{(\ell)} \leq 0$ inside the surface. A marginal surface therefore becomes the boundary of some trapped region in space, [see Wald, 1984]. Recall finally that a trapping horizon is then the 3-surface foliated by marginal surfaces. We can also make the definition more restrictive [Hayward, 2002, 1994], and require that the null normal n have negative expansion on the horizon, i.e. $\theta_{(n)} < 0$.

2.2 Gravitational Collapse

While the restriction of a problem to spherical symmetry is often made for the purpose of simplifying the underlying equations, in the case of gravitational effects affords us with an additional benefit: any physical disturbance that is spherically symmetrical with regards to some center cannot affect any observer interior to it by gravitational means. This familiar result from Newtonian gravity retains its validity in GR also. Therefore we may at times be free to ignore the existence of matter exterior to some region. Similarly, we may make use of the uniqueness of the vacuum Schwarzschild solution in spherical symmetry to treat the matter interior to some region as though it were concentrated at a point in the center.

2.2.1 Adiabatical Spherical Collapse

In order to discuss the collapse of a spherically symmetric distribution of matter it is necessary to start with the hydrodynamics that determine the collapse. The general result for a perfect fluid as formulated by Misner and Sharp [1964] begins with the prescription of the metric in comoving, synchronous coordinates. The spherical distribution can be built up conceptually from concentric spherical shells each labelled by a monotonically increasing parameter a , which we shall take to be equal to the number of baryons interior to the shell of areal radius r at time t_s , so that the worldline of a particular shell is given by $a(r, t_s)$. Furthermore, the Schwarzschild time coordinate t_s can be rescaled so that the metric can be written in the form:

$$ds^2 = -e^{2\Phi} dt^2 + \left(\frac{1}{\Gamma} \frac{\partial r}{\partial a} \right)^2 da^2 + r^2 d\Omega^2. \quad (2.19)$$

By choosing our coordinate system in this way we need to be careful with what is meant by a synchronous proper time coordinate. We define t to be the lapse of proper time on a particular shell since the initial state of the system, i.e., the arclength of the worldline of that particular shell as measured from the hypersurface $t = 0$. However, the choice of this hypersurface is arbitrary, so that the evolution of the space-time will appear different depending on how we perform this initial slicing. With that in mind, we can still discuss the invariants of the space-time without ambiguity.

Therefore, letting n to be the baryon number density and μ to be the average rest mass of baryons at a particular point, we can find a in terms of r by integrating over the number density n and proper volume $d\mathcal{V} = 4\pi r^2 \frac{1}{\Gamma} dr$, thus:

$$a = \int_0^r \frac{4\pi r^2 n}{\Gamma} dr. \quad (2.20)$$

Note that in this coordinate system we can easily accommodate the region outside of the matter distribution by foliating this region with shells comprising “imaginary” massless dust, so that $\mu = 0$.

In this comoving coordinate system, the fluid is at rest, so that the 4-velocity of the fluid is $u^\alpha = (e^{2\Phi}, 0, 0, 0)$. Baryon number conservation requires that $(nu^\alpha)_{;\alpha} = 0$. If we use the notation of Misner and Sharp that $\dot{q} = e^{-\Phi} \frac{\partial}{\partial t} q$, and $q' = \frac{\partial}{\partial a} q$, then this leads to the requirement that

$$\frac{\dot{\Gamma}}{\Gamma} = \frac{\dot{r}'}{r'} + \frac{(nr^2)'}{nr^2}. \quad (2.21)$$

A perfect fluid is one in which there are no shear stresses or dissipative forces. The stress-energy tensor for such a perfect fluid with energy density ρ and pressure

P is given by

$$T_{\alpha\beta} = (\rho + p)u_\alpha u_\beta + pg_{\alpha\beta}. \quad (2.22)$$

Here $\rho = \mu n$ for a fluid with particles having rest masses μ . We can calculate the mass-energy interior to shell a at time t by integrating over T_{tt} , thus

$$m = \int_0^a 4\pi r^2 \rho r' da. \quad (2.23)$$

The equation of local energy conservation, $T_{;\beta}^{\alpha\beta} = 0$, projected along the fluid's worldline, can be combined with the equation of baryon conservation to yield,

$$\dot{\rho} = \frac{\rho + p}{n} \dot{n}. \quad (2.24)$$

Additionally, the projection of the energy conservation equation perpendicular to u^α yields the relativistic Euler equation

$$(\rho + P)u^\alpha u_{\beta;\alpha} = -P_{;\beta} - u^\alpha P_{;\alpha} u_\beta, \quad (2.25)$$

from which we obtain

$$\Phi' = -\frac{P'}{\rho + P}. \quad (2.26)$$

[see Wheeler et al., 1973]. From the Einstein Field Equations we have that $G_{\alpha\beta} - 8\pi T_{\alpha\beta} = 0$. This leads to the result that

$$\Gamma^2 = 1 + \dot{r}^2 - \frac{2m}{r}, \quad (2.27)$$

and

$$r' \frac{\dot{\Gamma}}{\Gamma} = \Phi' \dot{r}. \quad (2.28)$$

See Appendix A.3 for details.

2.2.2 Pressure-Free Dust

The principal difficulty in including pressure in such an analysis is the formation of shock fronts resulting from the non-linearity of the equations. The system's energy tends to become concentrated into successively higher wavenumbers making a simple grid-based approach unfeasible. Additionally, the adiabaticity condition breaks down where shock fronts form so that artificial viscosities need to be introduced, somewhat by trial and error, in order to smooth out the shock transitions while still satisfying certain junction conditions. Thus the study of pressure-hindered gravitational collapse becomes a study of the hydrodynamics rather than of the relativity of the problem. For a detailed numerical treatment of the effects of pressure on gravitational collapse, see May and White [1966, 1967].

LeMaître-Tolman-Bondi Spacetime

In order to simplify our analysis and to obtain a parametric solution, we will consider the collapse in the absence of pressure, or where pressure is negligible. This situation is described by the so-called LeMaître-Tolman-Bondi spacetime family of solutions. For a review, see Bondi [1947] and Humphreys et al. [1998]. Setting $P = 0$ leads to $\Phi' = 0$, by equation 2.26, from which equation 2.28 implies that Γ is a function of a only. We can also set $\Phi = 0$ by requiring that the metric yield the Schwarzschild solution at infinity. From this t becomes a measurement of the comoving proper time rather than a rescaled time coordinate. These results can readily be used to analyze the collapse of shells of matter provided that m , the mass enclosed by a particular shell, remains constant during collapse. Equation 2.27 can then be rewritten as a

differential equation for r ,

$$\dot{r} = -\sqrt{\Gamma^2 + \frac{2m}{r}} - 1. \quad (2.29)$$

A parametric solution can be obtained as follows [see Gonçalves, 2001]:

$$t(\eta, a) = t_0(a) + mk^{-\frac{3}{2}}(\eta + \sin \eta), \text{ and} \quad (2.30a)$$

$$r(\eta, a) = \frac{2m}{k} \cos^2\left(\frac{\eta}{2}\right), \quad (2.30b)$$

where $k = 1 - \Gamma^2$ for readability, and η runs from η_0 to π , where η_0 is a constant to be determined, which will in general also depend on a . The time derivative of a shell's areal radius is given by

$$\dot{r} = \frac{dr}{d\eta} / \frac{dt}{d\eta} = -\sqrt{k} \tan\left(\frac{\eta}{2}\right). \quad (2.31)$$

To determine the value t_0 for each shell, we note that at $\eta = \eta_0$, $r = r_0$, the initial areal radius of the shell. As $t(\eta_0) = 0$, equation 2.30a yields

$$t_0(a) + mk^{-\frac{3}{2}}(\eta_0 + \sin \eta_0) = 0, \quad (2.32)$$

while η_0 is defined by equation 2.31,

$$r_0 = \frac{2m}{k} \cos^2\left(\frac{\eta_0}{2}\right),$$

so that

$$\eta_0(a) = 2 \arccos\left(\sqrt{\frac{kr_0}{2m}}\right). \quad (2.33)$$

We can also use equation 2.30a to define the time to collapse t_{col} for a particular shell by setting $\eta = \pi$, giving

$$t_{col}(a) = t(\pi, a) = t_0(a) + m\pi k^{-\frac{3}{2}}. \quad (2.34)$$

2.2.3 Locating the Trapping Horizon

Outward Null Geodesic Expansion

In order to calculate $\theta_{(\ell)}$ we need to define the tangent vector ℓ^α to the congruence, along with an auxiliary null tangent vector n^α for which $\ell_\alpha n^\alpha = 0$. Without obtaining an affine parameterization with which to define ℓ^α , we cannot use equation 2.14, so that we need to calculate \tilde{B}_α^α directly. Noting that $h_\mu^\alpha h_\alpha^\nu = h_\mu^\nu$, it follows that $\theta = h_\alpha^\beta l_{;\beta}^\alpha$. Then ℓ^α and n^α can be chosen as follows,

$$\ell^\alpha = \lambda(t, a) \left(1, \frac{\Gamma}{r'}, 0, 0 \right) \text{ and} \quad (2.35)$$

$$n^\alpha = \frac{1}{2\lambda(t, a)} \left(1, -\frac{\Gamma}{r'}, 0, 0 \right), \quad (2.36)$$

where $\lambda(t, a)$ is some arbitrary scaling function. We then obtain,

$$\theta_{(\ell)} = 2\lambda(t, a) \left(\frac{\Gamma + \dot{r}}{r} \right). \quad (2.37)$$

See Singh [1997] for an alternate derivation. Upon substituting in equation 2.31, we obtain

$$\theta_{(\ell)}(\eta, a) = 2\lambda \left(\frac{\Gamma - \sqrt{1 - \Gamma^2} \tan\left(\frac{\eta}{2}\right)}{r(\eta, a)} \right).$$

Therefore the equation that defines the trapping horizon is

$$\sqrt{1 - \Gamma^2} \tan(\eta/2) = \Gamma. \quad (2.38)$$

Note that we haven't made any requirement of $\theta_{(n)}$. However, it is easily verified that

$$\theta_{(n)} = 2\lambda(t, a) \left(\frac{-\Gamma + \dot{r}}{r} \right),$$

so that if $\theta_{(\ell)} = 0$, $\theta_{(n)}$ is automatically less than zero.

2.2.4 Initial Conditions

As our goal is to understand the evolution of trapping horizons rather than the hydrodynamics of a particular physical system, considerable freedom exists in the choice of initial conditions. However, relativity places certain fundamental constraints on these conditions which need to be considered. Furthermore, in choosing our coordinate system we have also made certain assumptions that in general may not universally apply.

When discussing initial conditions we may consider shells falling from rest or, more generally, collapsing with non-zero initial velocities. An ambiguity exists as to what these velocities are measured in reference to, since our coordinate system is by construction comoving. Mathematically, we simply think of the areal radius of a particular shell as a function of proper time along the worldline of that shell, so that the velocity is simply the derivative of this function with respect to proper time. Here, “velocity” is merely a label for \dot{r} , which is unrelated to the four-velocity of the shells, $v^\alpha = (1, 0, 0, 0)$. A stationary observer momentarily coincident with one of these shells (who happens to parameterize his space-time according to areal radius) will measure the space-like component of the shell's four-velocity to be $\frac{dr}{d\tau}$. However,

such an observer is by no means preferred by the physics, and may not even always be defined.

Furthermore, as mentioned earlier, what is meant by initial conditions is entirely dependent on our choice of initial hypersurface $t = 0$. Therefore, while we might specify that all shells start their collapse from rest, we can just as easily choose a hypersurface in which some shells have already evolved to the point where their velocities are finite, while others have yet to move. While no preferred slicing of space-time exists, in the case of a collapse starting from rest, we can think of the slicing as being one with time symmetry [Gonçalves, 2001].

Shell Crossing

Our treatment thus far has made use of the number of baryons interior to a shell as a label for that particular shell, and we have assumed that this coordinate is co-moving in that it remains constant throughout the shell's entire collapse. This assumption becomes invalid if infalling shells overtake one another during their collapse, and a *shell crossing singularity* or *shell focusing singularity* is said to occur. A shell crossing singularity is the set of points for which $\frac{\partial r}{\partial a} = 0$ and $r > 0$, i.e. r is no longer a monotonically increasing function of a , while a shell focusing singularity occurs similarly at $r = 0$. The condition under which shell-crossing occurs is equivalent to $t'_{coll} < 0$ [Gonçalves, 2001].

When dealing with inhomogeneous density distributions, considerable effort is needed to find a suitable density function that both approximates the situation we want to study and avoids these shell-crossing singularities. For a distribution collapsing from rest, $t'_{coll} > 0$ implies

$$\frac{1}{m} \frac{dm}{dr_0} < \frac{3}{r_0}. \quad (2.39)$$

However, looking at equation 3.2, it is evident that we can satisfy this requirement by choosing $m(r_0) = r_0^3 \tilde{m}(r_0)$ where $\tilde{m}(r_0)$ is some monotonically decreasing function of r_0 so that

$$t_{col}(r_0) = \pi \frac{1}{\sqrt{8\tilde{m}}}, \quad (2.40)$$

is in-turn a monotonically increasing function of r_0 . This can be a useful aid in determining whether a particular distribution will be well behaved.

Coordinate Singularities

Additional care has to be taken when specifying the initial conditions of the matter distribution. Specifically, the density and velocity profile must be chosen so that Γ remains real and nonzero throughout the region being studied. Each shell of initial areal radius r_0 and initial velocity \dot{r}_0 containing mass $m(r_0)$ has an associated radius r_m defined by $1 + \dot{r}^2 - \frac{2m(r)}{r_m} = 0$. For the coordinate system to remain regular, r must be greater than r_m .

Furthermore, we must also ensure that infalling shells begin their collapse on timelike curves, so that we may choose a space-like hypersurface that is everywhere orthogonal to these curves as our initial slicing of the space-time. This is equivalent to specifying \dot{r}_0 such that $ds^2 < 0$ for vectors tangent to those geodesics. This is especially important near $r = r_m$ where $\Gamma \rightarrow 0$ so that ds^2 becomes highly sensitive to \dot{r}_0 .

Chapter 3

Analytical Treatment

While the baryon parameter a is a useful coordinate for obtaining solution parameters, the initial areal radius r_0 is more suitable for calculation purposes, although either serves as a good shell label.

3.1 Collapse From Rest

3.1.1 Inhomogeneous Collapse

Some important features of the gravitational collapse can be seen in the restricted case when all shells begin their collapse from rest. Consider an isolated spherical distribution of total mass M and initial radius R_0 . Since the collapse is starting from rest we must have that $R_0 > 2M$, and in general that $r_0 > 2m(r_0)$ for all shells. If any part of the distribution were contained entirely within its gravitational radius $2m$, there could not be any stationary frames inside it, as it would constitute a black hole.

We can analyse both the regions inside and outside the distribution by extending our coordinate system beyond R_0 and taking $\mu(r_0) = 0$ for $r_0 > R_0$. The shells outside

the distribution are therefore massless and serve only as coordinate identifiers. The evolution of each shell is given by equations 2.30a and 2.30b. Since $\dot{r} = 0$ when $\eta = 0$, it follows that $\eta = 0$ coincides with $t = 0$. These equations then reduce to

$$t(\eta, r_0) = \sqrt{\frac{r_0^3}{8m}}(\eta + \sin \eta), \text{ and} \quad (3.1a)$$

$$r(\eta, r_0) = r_0 \cos^2 \left(\frac{\eta}{2} \right). \quad (3.1b)$$

By equation 2.34, each shell reaches the singularity in a time given by,

$$t_{col}(r_0) = t(\pi, r_0) = \pi \sqrt{\frac{r_0^3}{8m}}. \quad (3.2)$$

The equation that defines the trapping horizon is therefore

$$\sqrt{\frac{2m}{r_0}} \tan \left(\frac{\eta}{2} \right) = \sqrt{1 - \frac{2m}{r_0}}, \quad (3.3)$$

or equivalently,

$$\eta_{TH} = 2 \arctan \left(\sqrt{\frac{r_0}{2m} - 1} \right). \quad (3.4)$$

Consider what happens once the entire mass M has collapsed to within its gravitational radius. Equation 2.38 states that a particular shell will intersect the trapping horizon if and where $\tan \left(\frac{\eta}{2} \right) = \frac{\Gamma}{\sqrt{1-\Gamma^2}}$ holds for that shell. Each shell initially outside the matter distribution has $k = \frac{2M}{r_0}$, so that equation 2.30b gives the location of the

marginal surface to be

$$\begin{aligned}
r(r_0) &= \frac{r_0}{1 + \tan^2\left(\frac{\eta}{2}\right)} \\
&= r_0 (1 - \Gamma^2) \\
&= r_0 k \\
&= 2M.
\end{aligned} \tag{3.5}$$

Thus all exterior shells which do intersect the trapping horizon do so at the same radius $r = 2M$, which is also the event horizon of the newly formed black hole.

We can also ask whether, in addition to the marginal surface that forms at $r = 2M$, there may be other such surfaces that form or vanish inside the matter distribution. Consider therefore the situation in which the distribution begins its collapse on the verge of forming a black hole so that initially $R_0 = 2M + \varepsilon$ where ε is an arbitrarily small positive value. Since $k = \frac{2m}{r_0}$, the analysis leading up to equation by equation 3.5 similarly yields,

$$r_{TH}(r_0) = 2m(r_0). \tag{3.6}$$

We can further combine equations 3.1a and 3.4 to determine the time $t_{TH}(r_0)$ at which the marginal surface forms. From equation 3.6 it is apparent that were the collapse allowed to continue, each shell would eventually form a marginal surface where, in the absence of any additional infalling matter, we would normally think of an event horizon as having been formed.

Another question which arises is whether the two solutions found thus far are contiguous with one another, and in general, whether these solutions are continuous at all. In the absence of shell crossing, each shell of initial radius r_0 defines a single point $(t_{TH}(r_0), r_{TH}(r_0))$ on the trapping horizon. Therefore the continuity of the trapping

horizon rests in part on the continuity of $m(r_0)$. We must also have continuity in the value $t_{TH}(r_0)$, or, equivalently, in the value $\eta_{TH}(r_0)$. Combining equations 3.1a and 3.1b with equation 3.6 yields,

$$\eta_{TH}(r_0) = 2 \arccos \left[\sqrt{\frac{2m(r_0)}{r_0}} \right]. \quad (3.7)$$

Therefore the continuity of $m(r_0)$, in addition to the requirement that $r_0 < 2m(r_0)$, determines the continuity of $t_{TH}(r_0)$.

3.1.2 Oppenheimer-Snyder Collapse

In the case of a homogeneous distribution collapsing from rest, ρ is constant everywhere inside the distribution, so that $m = \frac{4}{3}\pi\rho r^3$. Therefore, by equation 2.34, $t_{col} = \frac{1}{4}\sqrt{\frac{3\pi}{2\rho}}$, so that all shells collapse in the same finite comoving proper time.

Because $t(\eta)$ does not depend on r , the Oppenheimer-Snyder model is especially suited for taking spacelike cross-sections of the space time; i.e. surfaces of constant η are also surfaces of constant time. By making use of equations 3.1a and 3.1b, we can easily obtain η and r_0 at a particular point in the space-time where these equations are defined. While equation 3.1a has to be inverted numerically, equation 3.1b can easily be inverted once η is known. Most quantities of interest, including the metric itself, can then be calculated.

For instance, we may wish to trace the paths of outgoing null geodesics explicitly. This can be done by numerically solving the differential equation $\frac{dr}{dt} = \Gamma(r, t)^2$ using suitable initial conditions. Γ can be obtained at each point in the iteration by first calculating η and then r_0 , finally substituting these values into equation 2.27.

3.2 General Inhomogeneous Collapse

In the case that shells do not begin their collapse from rest, $\eta = 0$ no longer coincides with $t = 0$, so that equation 3.1a becomes invalid. However, we can again begin our analysis starting from equation 2.38. In the case of general inhomogeneous collapse, we have that $\Gamma(r_0) = \sqrt{1 + \dot{r}_0^2 - \frac{2m}{r_0}}$ so that $k = 1 - \Gamma^2 = \frac{2m}{r_0} - \dot{r}_0^2$, therefore

$$\tan\left(\frac{\eta_{TH}}{2}\right) = \sqrt{\frac{1}{\dot{r}_0^2 + \frac{2m(r_0)}{r_0}} - 1}, \quad (3.8)$$

and

$$\begin{aligned} r_{TH}(r_0) &= \frac{2m}{k} \cos^2\left(\frac{\eta_{TH}(r_0)}{2}\right) \\ &= \frac{2m}{k} \left[1 + \tan^2\left(\frac{\eta_{TH}(r_0)}{2}\right)\right]^{-1} \\ &= 2m(r_0), \end{aligned} \quad (3.9)$$

reproducing equation 3.6.

While the validity of this result in the general case is not entirely surprising, the reasons for this generality are more subtle. In effect the radius at which a particular shell forms a marginal surface is entirely determined by the gravitational effect of all shells interior to it (because of spherical symmetry), which in turn is determined solely by $m(r)$. We can see this by imagining cutting away the outer layers of the distribution (which have no effect on the geometry of our chosen shell). The metric at this point should then correspond to the Schwarzschild metric, which is determined by $m(r)$. Then since $\theta_{(\ell)}$ depends only on the metric and the choice of ℓ^α , we see that the shell velocities do not enter into the location of the marginal surface. Specifying a non-zero initial velocity merely changes the time t_{TH} at which a shell forms a marginal surface.

3.3 Classification

Once the trapping horizon is located, its signature can be calculated by determining the norm of any tangent vector lying on its surface. Since this surface can be parameterized in an arbitrary way, it is only the sign of this value that is important.

The trapping horizon can be seen as the surface on which $r(t, r_0) - 2m(t, r_0)$ becomes zero, so that the normal one-form to this surface is given by $\nabla_\alpha(r - 2m)$ evaluated at $r = 2m$. The tangent vector v^α to the surface is defined by $v^\alpha \nabla_\alpha(r - 2m) = 0$ [Booth, 2005], so

$$\begin{aligned} v^t \dot{r} + v^{r_0} (\partial_{r_0} r - 2\partial_{r_0} m) &= 0 \\ v^{r_0} &= -v^t \left(\frac{\dot{r}}{\partial_{r_0} r - 2\partial_{r_0} m} \right), \end{aligned} \tag{3.10}$$

and therefore

$$\begin{aligned}
\|v\|^2 &= g_{\alpha\beta}v^\alpha v^\beta \\
&= (v^t)^2 \left(-1 + \frac{(\partial_{r_0}r)^2}{1-k} \frac{\dot{r}^2}{(\partial_{r_0}r - 2\partial_{r_0}m)^2} \right) \\
&= (v^t)^2 \left(-1 + \frac{1}{(1 - 2\frac{\partial_{r_0}m}{\partial_{r_0}r})^2} \right) \\
&= (v^t)^2 4\rho A \frac{1 - \rho A}{(1 - 2\rho A)^2},
\end{aligned}
\tag{3.11}$$

where we have used the fact that $\dot{r}^2 = 1 - k$ on the trapping horizon, and that $\partial_{r_0}m = A\rho\partial_{r_0}r$ where A is the area of the shell. Therefore we can determine whether the horizon is spacelike, timelike, or null, depending on the sign of $1 - \rho A$. The term $\partial_{r_0}r$ can be calculated explicitly by differentiating equation 2.30b with respect to r_0 while holding t fixed, keeping in mind that η depends on r_0 , according to equation 2.30a, which can in turn be used to determine $\partial_{r_0}\eta$.

Chapter 4

Results

4.1 Oppenheimer-Snyder Collapse

In order to become familiar with some of the general features of gravitational collapse it is instructive to examine the Oppenheimer-Snyder model in more detail. Starting with a distribution of uniform density $\rho = 1$ collapsing from rest, it is easily verified that $r_0 = 2m(r_0)$ at $r_0 = r_{OS} = \sqrt{3/8\pi} \approx 0.345$. Since we cannot have stationary reference frames inside this radius once a black hole has already formed, we can either extend the matter distribution beyond this radius and restrict our analysis to this exterior region, or we can truncate the matter distribution at some point inside this radius thereby specifying “innocuous” initial conditions. The former approach presents some difficulties since Γ is undefined here, and does not provide significantly more insight to the model than the latter. Therefore we may choose the boundary of our matter distribution to lie at some point interior to r_m , say $R = 0.95r_{OS} \approx 0.328$.

The collapse of this distribution is shown in Figure 4.1. Note that in this case all shells reach the singularity at $t_{col} = \frac{1}{4}\sqrt{3\pi/2\rho} \approx 0.543$. The bold curve indicates the location of the trapping horizon. The straight horizontal segment of the trapping

horizon coincides with $r = 2M$, and forms once the distribution has collapsed to within its gravitational radius. This segment of the trapping horizon also forms part of the event horizon for the system.

The sign of $\theta_{(\ell)}$ is also indicated for each of the regions separated by the trapping horizons. Initially, $\theta_{(\ell)} \rightarrow +\infty$ as $r \rightarrow 0$, while $\theta_{(\ell)} \rightarrow 0$ as $r \rightarrow \infty$. This can be understood from a purely geometrical argument: Near the centre of the distribution, $m(r)$ is small so that gravity has little effect on the expansion of outgoing lightrays. As $r \rightarrow 0$, area A grows as r^2 while dA grows as r , so that $\theta_{(\ell)} \sim dA/A \sim r/r^2 = 1/r$. Similarly, far away from the distribution the metric is approximately flat so that $\theta_{(\ell)} \sim 1/r \rightarrow \infty$ [Booth, 2005].

Once the distribution has become sufficiently dense, gravitational effects become more significant. In the Oppenheimer-Snyder case, a singularity does not form until all shells reach $r = 0$ simultaneously, so that $m(r)$ remains small near the centre. Therefore the two limits discussed above still hold true. However, a region where $\theta_{(\ell)} < 0$ forms between these two limits, as indicated in the figure, once the gravitational effects begin to dominate.

4.2 Inhomogeneous Collapse from Rest

4.2.1 Single Pulse Falling into a Black Hole

While the Oppenheimer-Snyder case is perhaps the simplest solution we can study, it obscures much of the dynamics we wish to study. The homogeneity and isotropy conditions are more suited to cosmological models than to stellar collapse, which generally has lower symmetry. Instead, we can look at perturbations to an already formed trapping horizon. This can be done by choosing a matter distribution $m(r_0)$

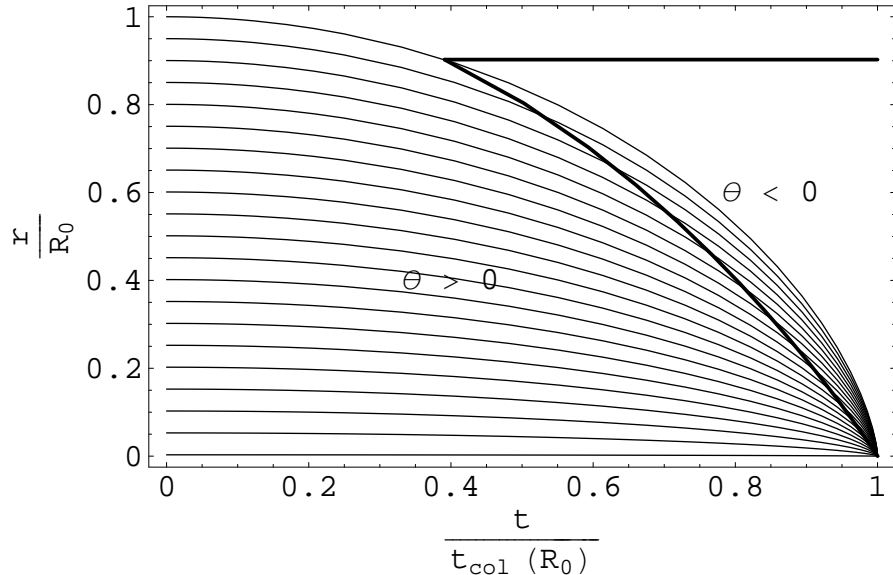


Figure 4.1: Collapse of 20 concentric shells in the Oppenheimer-Snyder model is shown here. The areal radius of each shell is plotted as a function of comoving proper time. $R_0 \approx 0.328$ and $\rho = 1$. All shells reach the singularity at $t_{col}(R_0) \approx 0.543$. The trapping horizon is indicated by the bold curve.

with a singularity at $r = 0$, i.e., a constant term, and a localized gradient corresponding to a diffuse spherical pulse of infalling matter. We can place the bulk of the pulse outside of the marginal surface formed by the singularity, so that this part of the trapping horizon converges with the event horizon in the distant past (when a null ray has sufficient time to escape the infalling pulse).

A suitable mass function which makes use of a Gaussian radial density is given by

$$m(r_0) = m_A + m_B \int_0^{r_0} \frac{1}{\sqrt{\pi}} e^{-(x-r_p)^2} dx, \quad (4.1)$$

where m_A is the mass of the singularity, m_B determines the mass of the pulse, and r_p determines the initial radius of the pulse. The function $m(r_0)$ is easily integrated by making use of the error function. The density and mass profiles for this distribution are shown in Figures 4.2 (a) and (b), while the conditions that determine the regularity

of the solutions are shown in Figures 4.2 (c) and (d). In this case the effect of a low-density pulse on the trapping horizon was studied.

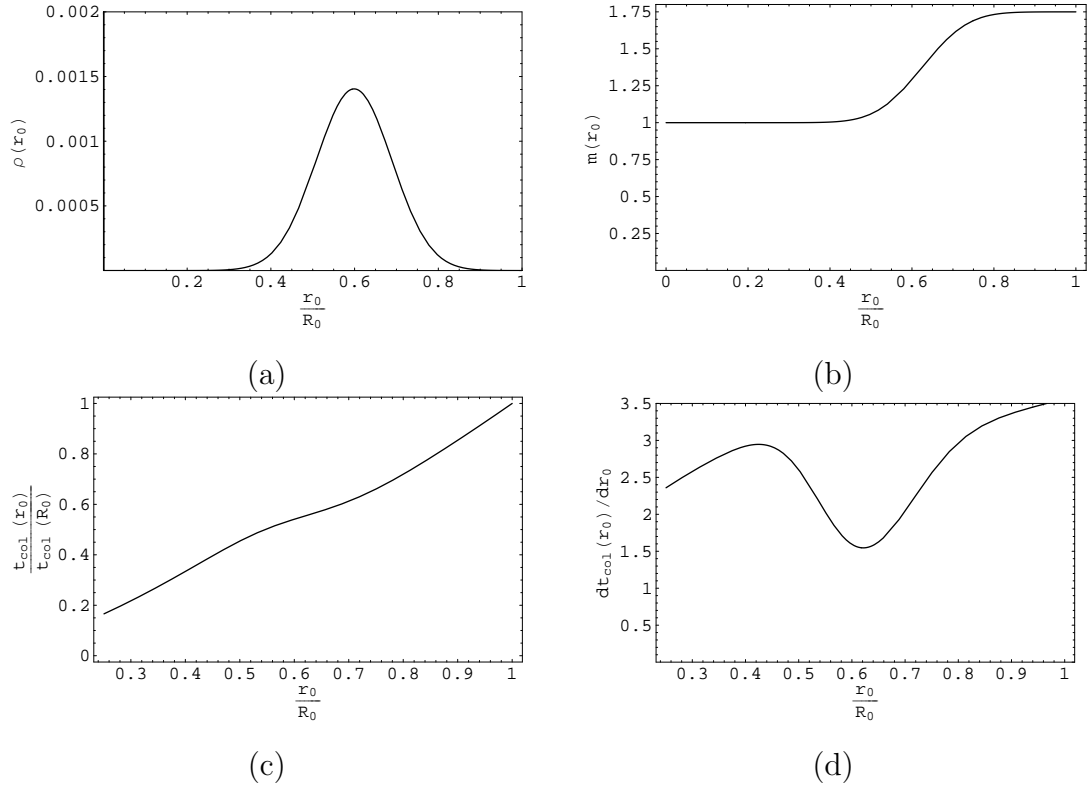


Figure 4.2: The density and mass profiles for the mass distribution given by $m(r_0) = 1 + \int_0^{r_0} \frac{3}{4\sqrt{\pi}} e^{-(x-5)^2} dx$ is shown in (a) and (b) respectively, while it is verified that shell crossing does not occur as can be seen in (c) and (d).

Figure 4.3 shows the collapse of this matter distribution, as well as the evolution of the trapping horizon. As expected, the trapping horizon converges with the event horizon at times well separated from the collapse event. The trapping horizon grows continuously between these two limits, and the most pronounced expansion occurs as the pulse reaches its gravitational radius.

The expansion can be understood in two ways. As the density of the system increases, more mass is contained within its gravitational radius, moving the marginal surface (where $r = 2m(r_0)$) outwards. On the other hand, as the mass contained within shells increases steadily as r_0 increases, the time needed for outer shells to reach their gravitational radii is reduced, pulling the trapping horizon backward. While this second interpretation is more geometrical than the first, it has the benefit of treating the trapping horizon as a single three-dimensional surface weaving through spacetime rather than a collection of two-dimensional marginal surfaces expanding and shrinking, disappearing and reappearing from time to time.

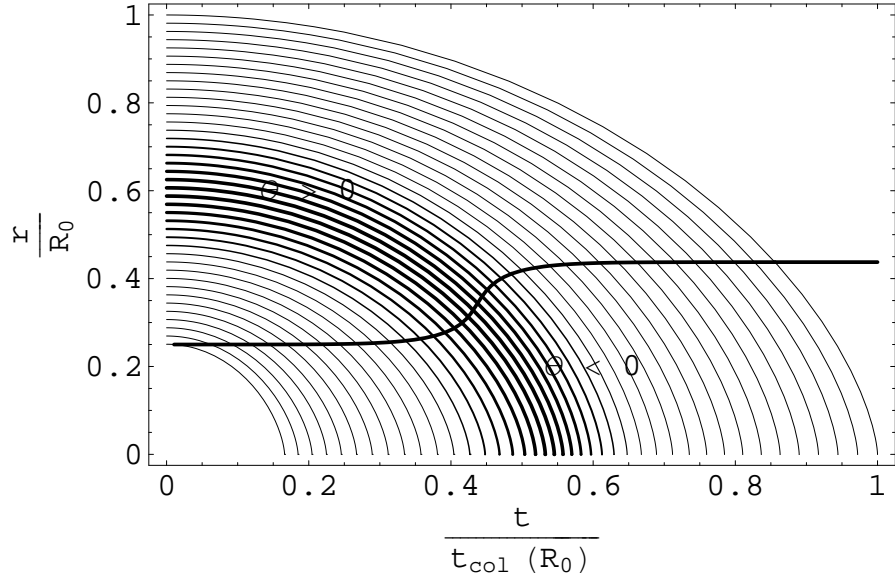


Figure 4.3: Collapse of 40 concentric shells is plotted for the mass distribution given by $m(r_0) = 1 + \int_0^{r_0} \frac{3}{4\sqrt{\pi}} e^{-(x-5)^2} dx$. The areal radius of each shell is plotted as a function of comoving proper time. The trapping horizon is indicated by the bold curve.

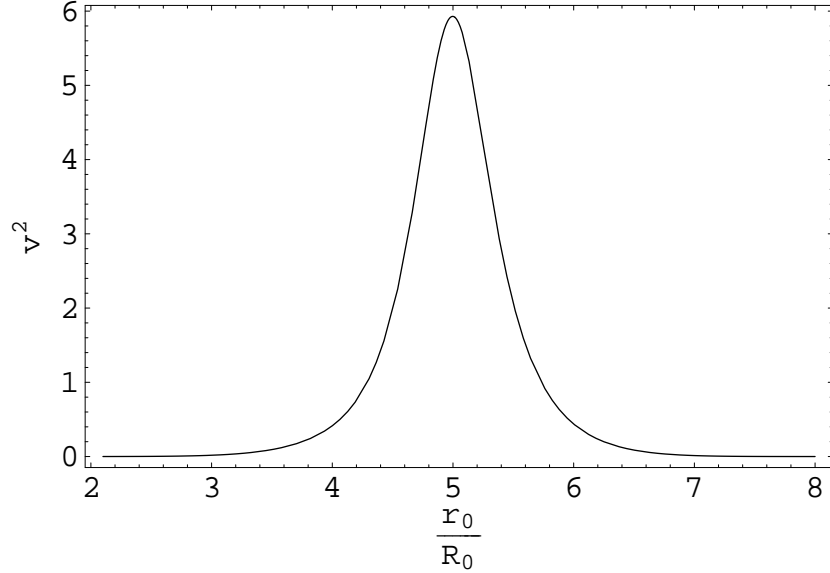


Figure 4.4: The signature $\|v\|^2$ of the trapping horizon formed by the mass distribution $m(r_0) = 1 + \int_0^{r_0} \frac{3}{4\sqrt{\pi}} e^{-(x-5)^2} dx$, which describes concentric infalling shells, is shown here as a function of initial radius r_0 .

To illustrate what is meant by the trapping horizon being pulled backward by the infalling matter, we can look at the same density profile as in the previous example, but with a significantly more massive pulse (in fact, the most massive the model will support before shell crossing occurs). Again, the density and mass profiles are shown in Figures 4.5 (a) and (b), while the regularity conditions are shown in Figures 4.5 (c) and (d). As can be seen in Figure 4.5 (d), this density profile just barely avoids the onset of shell crossings.

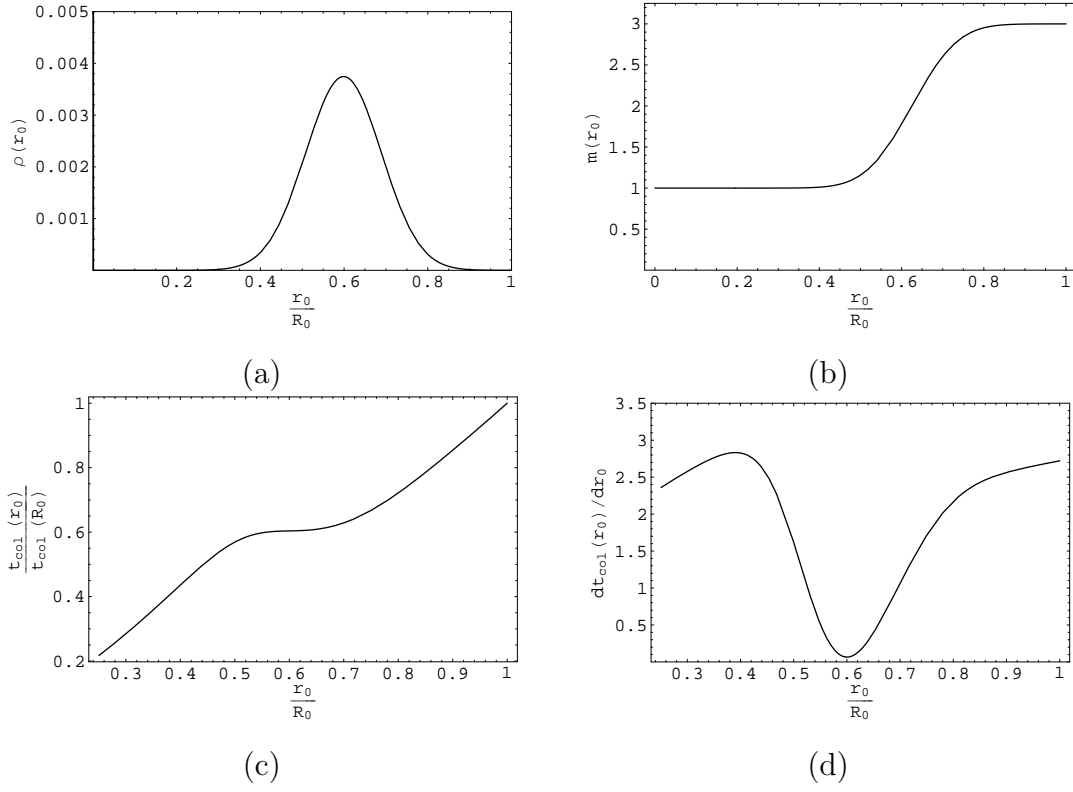


Figure 4.5: The density and mass profiles for the mass distribution given by $m(r_0) = 1 + \int_0^{r_0} \frac{2}{\sqrt{\pi}} e^{-(x-5)^2} dx$ is shown in (a) and (b) respectively, while it is verified that shell crossing does not occur as can be seen in (c) and (d).

Looking at Figure 4.6, we see that the distortion of the trapping horizon is particularly pronounced. As in the Oppenheimer-Snyder case, an untrapped pocket (denoted by $\theta > 0$) is created inside the outer gravitational radius, which can be understood from geometrical considerations. While observers in this region may not be inside marginal surfaces, they may nevertheless be destined to fall inwards if they cannot escape the pocket before it shrinks to zero size.

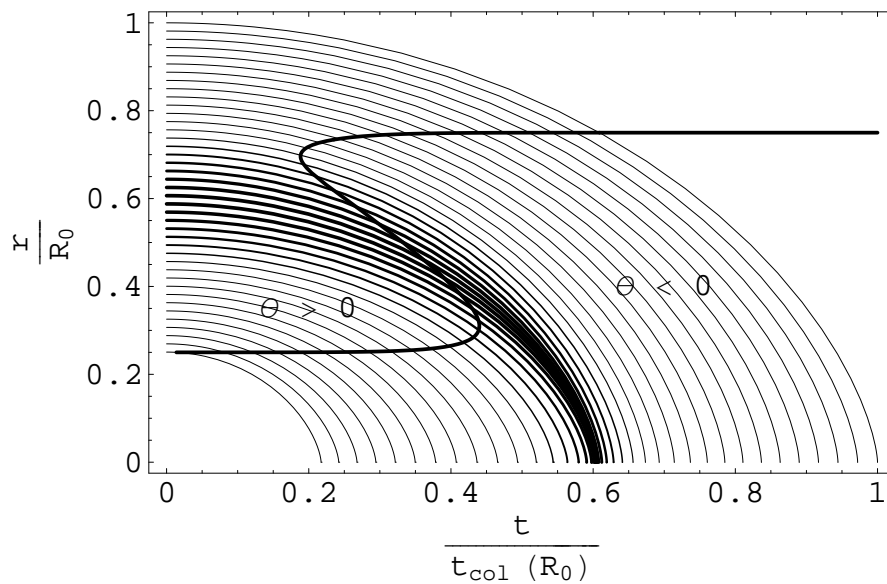


Figure 4.6: Collapse of 40 concentric shells is plotted for the mass distribution given by $m(r_0) = 1 + \int_0^{r_0} \frac{2}{\sqrt{\pi}} e^{-(x-5)^2} dx$. The areal radius of each shell is plotted as a function of comoving proper time. The trapping horizon is indicated by the bold curve.

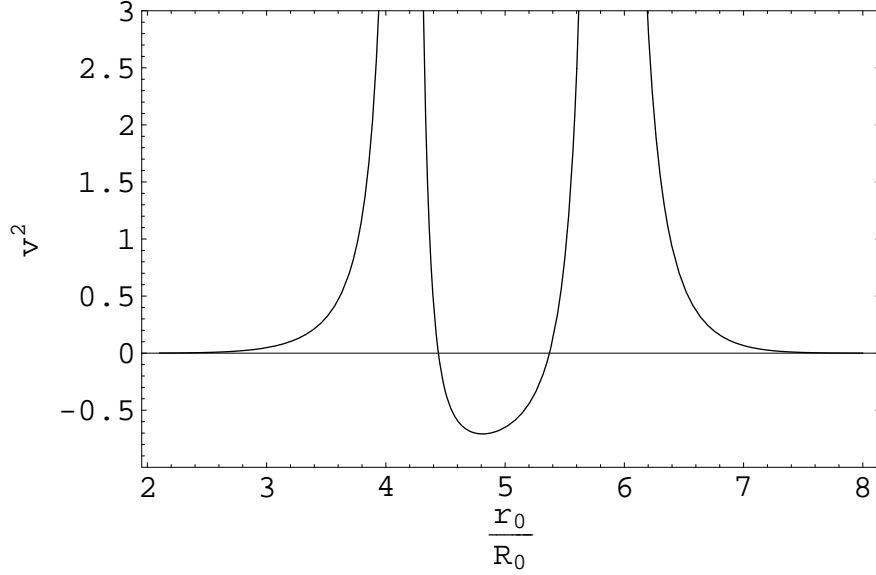


Figure 4.7: The signature $\|v\|^2$ of the trapping horizon formed by the mass distribution $m(r_0) = 1 + \int_0^{r_0} \frac{2}{\sqrt{\pi}} e^{-(x-5)^2} dx$, which describes concentric infalling shells, is shown here as a function of initial radius r_0 .

For completeness, Figures 4.8 (a) through (c) and 4.9 summarize the same situation for a range of masses from $m_B = 0$, where no pulse exists, to $m_B = 2$, the case previously considered.

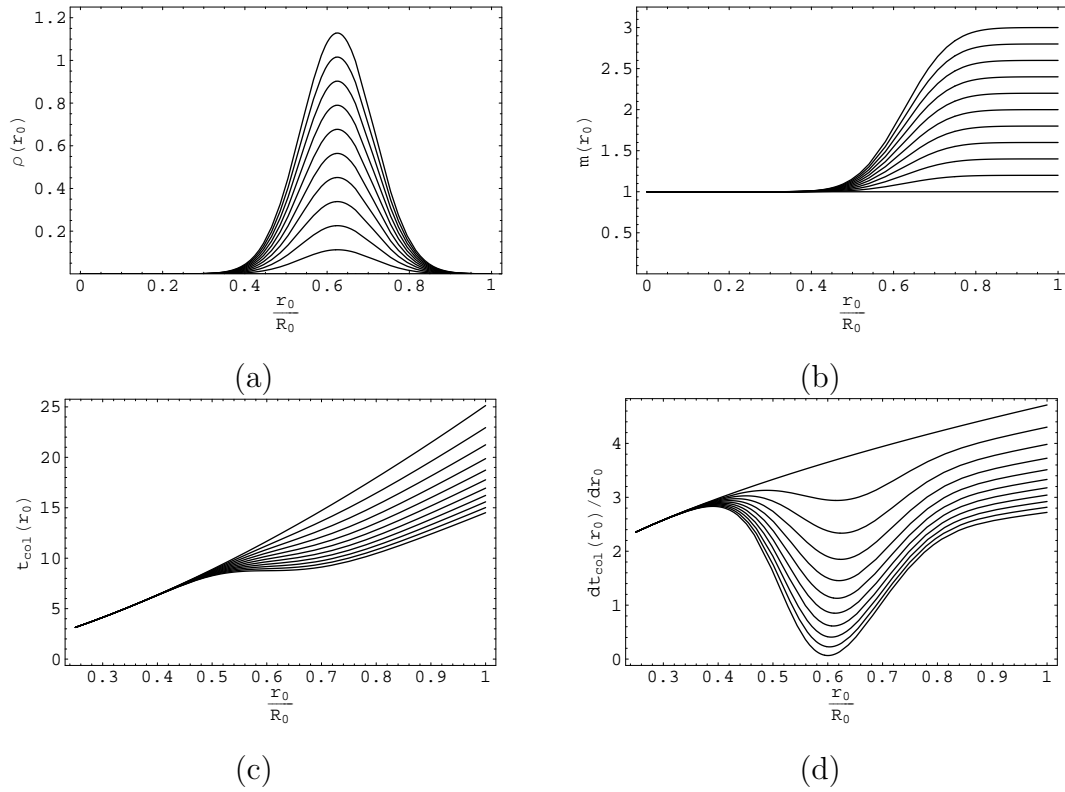


Figure 4.8: The density and mass profiles for the mass distributions given by $m(r_0) = 1 + \int_0^{r_0} m_B \frac{1}{\sqrt{\pi}} e^{-(x-5)^2} dx$ is shown in (a) and (b) respectively, while it is verified that shell crossing does not occur as can be seen in (c) and (d). Here m_B ranges between 0 (no pulse) and 2 (an extremely massive pulse).

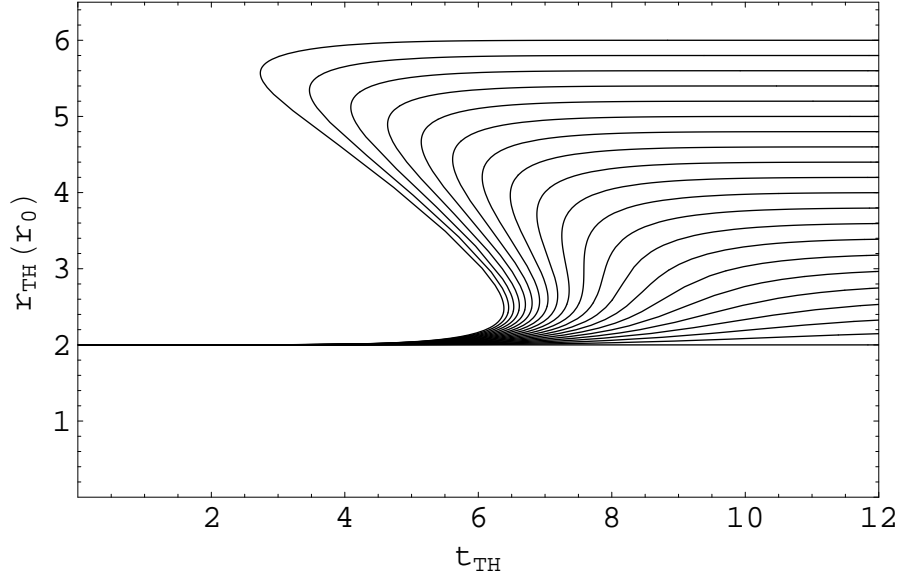


Figure 4.9: Trapping horizons resulting from various masses of infalling pulses are shown here. The mass distributions are described by $m(r_0) = 1 + m_B \int_0^{r_0} \frac{1}{\sqrt{\pi}} e^{-(x-5)^2} dx$ where m_B ranges between 0 and 2. The areal radius of trapping horizon is plotted as a function of time.

4.2.2 Concentric Infalling Shells

We can see how the trapping horizon evolves when multiple concentric shells of matter are allowed to collapse from rest by choosing \tilde{m} to contain multiple steps in a somewhat regular fashion. This can be done, by no means uniquely, by choosing \tilde{m} for instance to be:

$$\tilde{m}(r_0) = m_A - m_B \int_0^{r_0} \sin^2(\alpha x) dx, \quad (4.2)$$

where m_A and m_B specify the strengths of the gravitational sources, while α is a scaling parameter. The density and mass profiles for this distribution are shown in Figures 4.10 (a), and (b), while t_{col} and $\frac{dt_{col}}{dr_0}$ are shown in Figures 4.10 (c), and (d). Note also that $t_{col}(r_0)$ contains several plateaus so that multiple shell-focusing events will occur during the collapse.

The collapse of this distribution is shown in Figure 4.11. While the collapse is

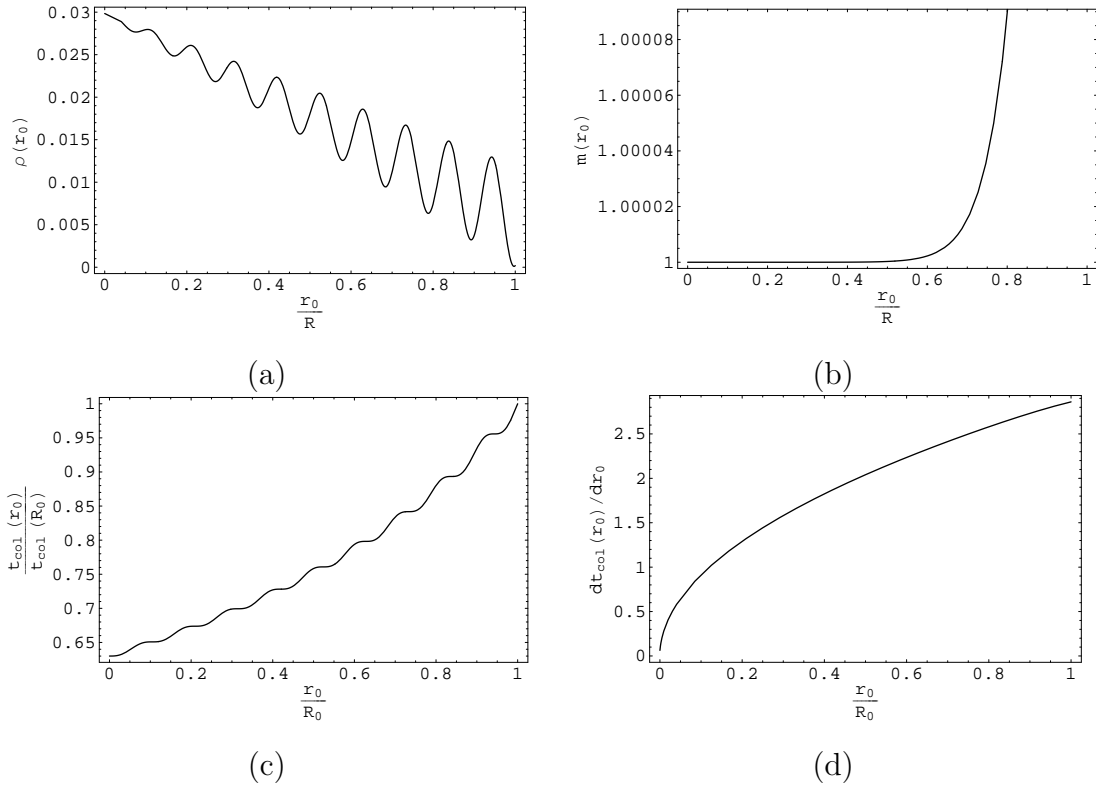


Figure 4.10: The density and mass profiles for the mass distribution given by $m(r_0) = r_0^3 (0.125 - 0.05 \int_0^{r_0} \sin^2(10x) dx)$ is shown in (a) and (b) respectively, while it is verified that shell crossing does not occur as can be seen in (c) and (d). Here R_0 , the radius of the outermost shell, is taken to be 3

qualitatively similar to the Oppenheimer-Snyder collapse (see Figure 4.1), each shell reaches the singularity in a different comoving proper time. We can think of the trapping horizon as being dragged along with the infalling mass as local variations in density tend to accelerate or delay the onset of the trapping horizon at a particular radius (See Equations 3.1a and 3.7). Also note the occurrence of several shell-focusing events during the late stages of the collapse, as predicted by Figure 4.10.

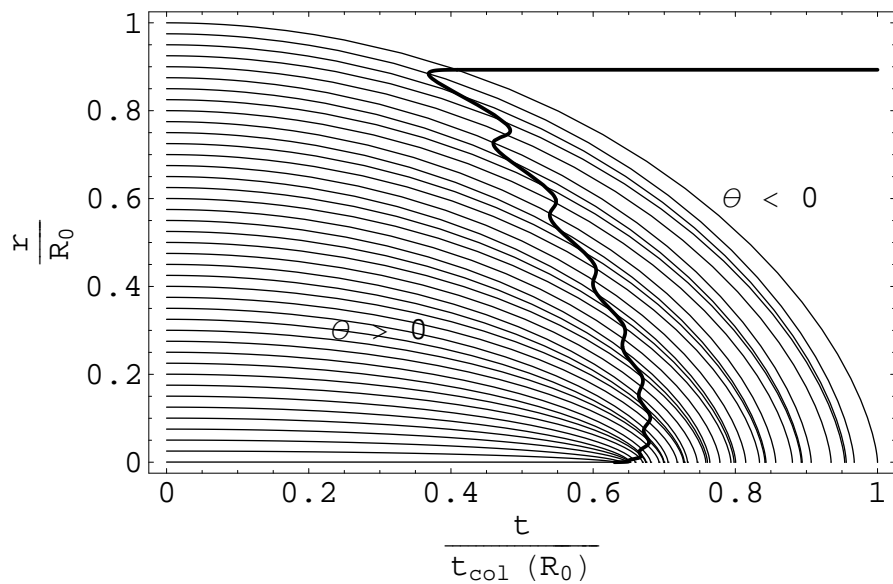


Figure 4.11: Collapse of 40 concentric shells is plotted for the mass distribution given by $m(r_0) = r_0^3 (0.125 - 0.05 \int_0^{r_0} \sin^2(10x) dx)$. The areal radius of each shell is plotted as a function of comoving proper time. The trapping horizon is indicated by the bold curve.

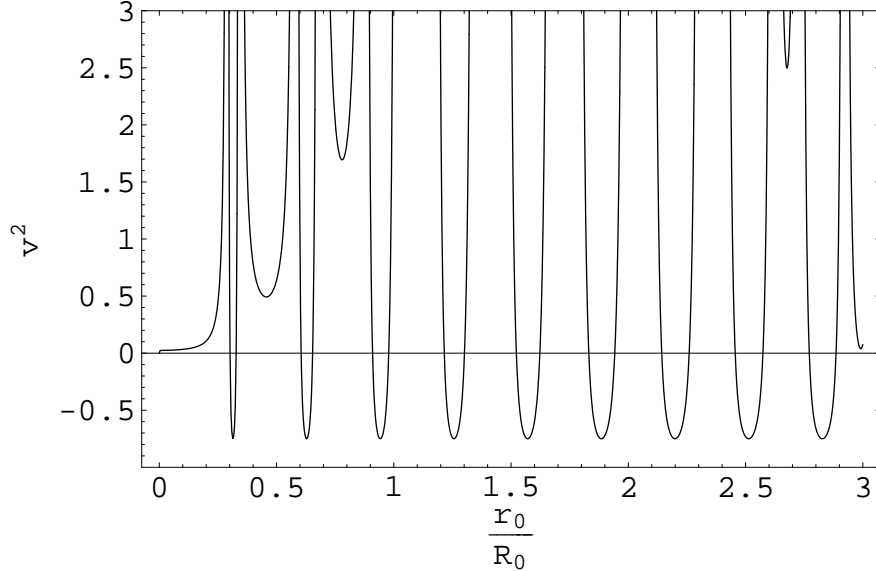


Figure 4.12: The signature $\|v\|^2$ of the trapping horizon formed by the mass distribution $m(r_0) = r_0^3 (0.125 - 0.05 \int_0^{r_0} \sin^2(10x) dx)$, which describes concentric infalling shells, is shown here as a function of initial radius r_0 .

We can also model a set of concentric infalling pulses of matter with a density function of the form $\rho \sim \sin^2(r_0)$. However, for large values of r_0 , we would expect that $m(r_0) \sim r_0^3$, so that $\tilde{m}(r_0)$ cannot be monotonically decreasing, but instead oscillates around a central value. Choosing $\rho \sim \frac{1}{r_0} \sin^2(r_0)$ gives approximately the correct behaviour at large values of r_0 , while $\rho \sim \frac{1}{r_0^2} \sin^2(r_0)$ gives the correct behaviour at all scales (and remains finite as $r_0 \rightarrow 0$). Furthermore, to ensure that the condition $r_0 > 2m(r_0)$ is satisfied, an appropriate scaling factor must be chosen. Taking $\rho = \frac{\alpha}{r_0^2} \sin^2(\beta r_0)$, we get that

$$m(r_0) = \frac{\alpha}{2} r_0 - \frac{\alpha}{4\beta} \sin(2\beta r_0), \quad (4.3)$$

while

$$r_0 - 2m(r_0) = (1 - \alpha)r_0 + \frac{\alpha}{2\beta} \sin(2\beta r_0), \quad (4.4)$$

so that we must require that $\alpha < 1$. In general the requirement that $r_0 > 2m(r_0)$ will not be satisfied near the origin, where the sinusoidal term dominates. However, we can merely exclude this region from our analysis.

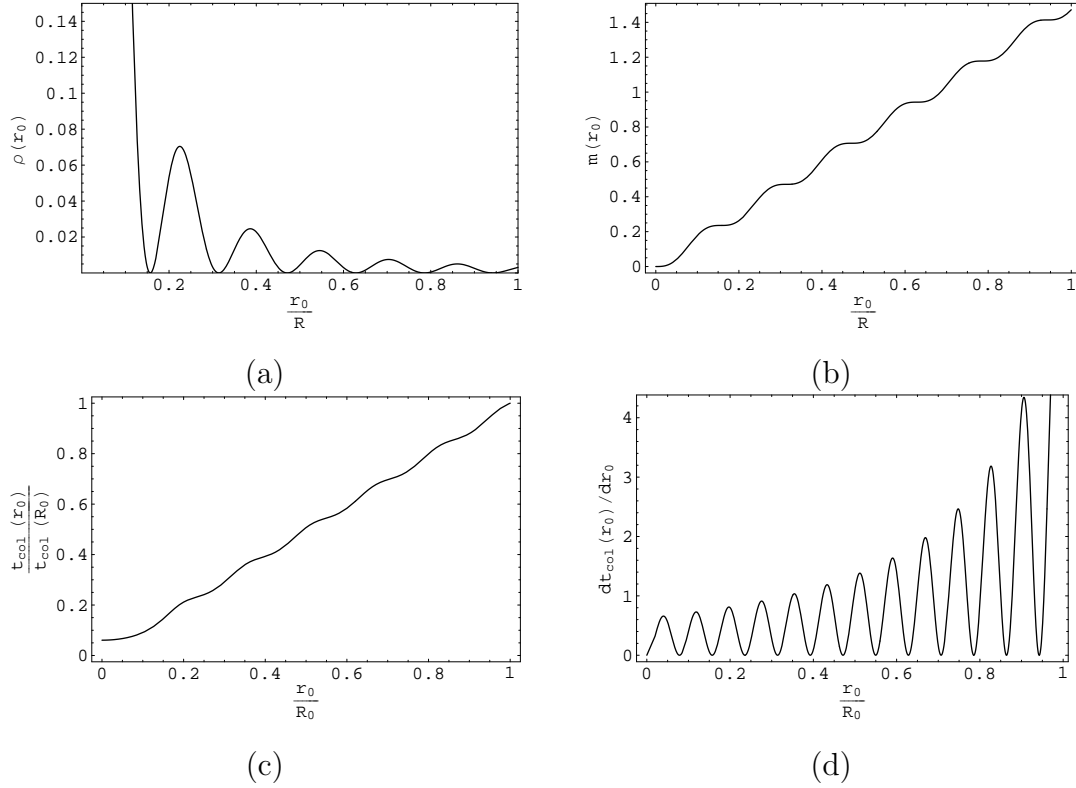


Figure 4.13: The density and mass profiles for the mass distribution given by $m(r_0) = 0.75 \int_0^{r_0} \sin^2(5x) dx$ is shown in (a) and (b) respectively, while it is verified that shell crossing does not occur as can be seen in (c) and (d).

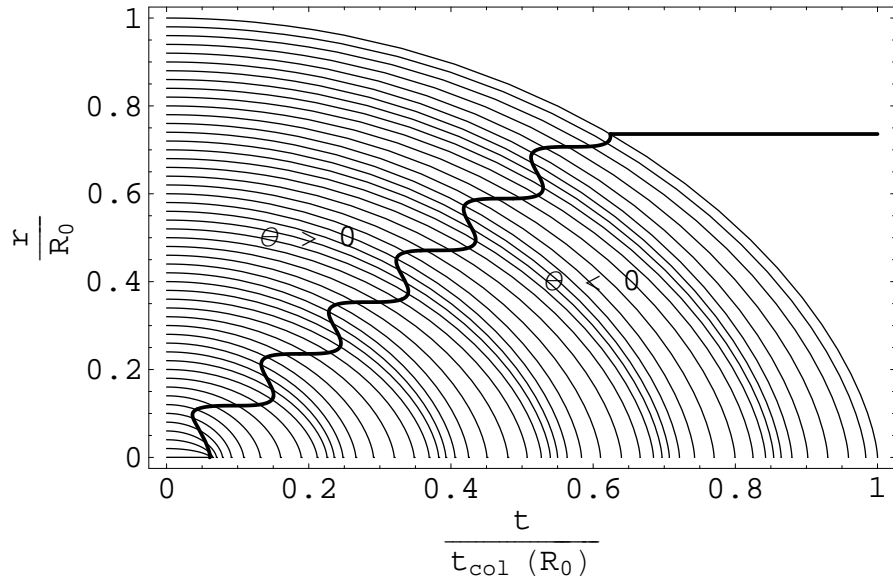


Figure 4.14: Collapse of 40 concentric shells is plotted for the mass distribution given by $m(r_0) = 0.75 \int_0^{r_0} \sin^2(5x) dx$. The areal radius of each shell is plotted as a function of comoving proper time. The trapping horizon is indicated by the bold curve.

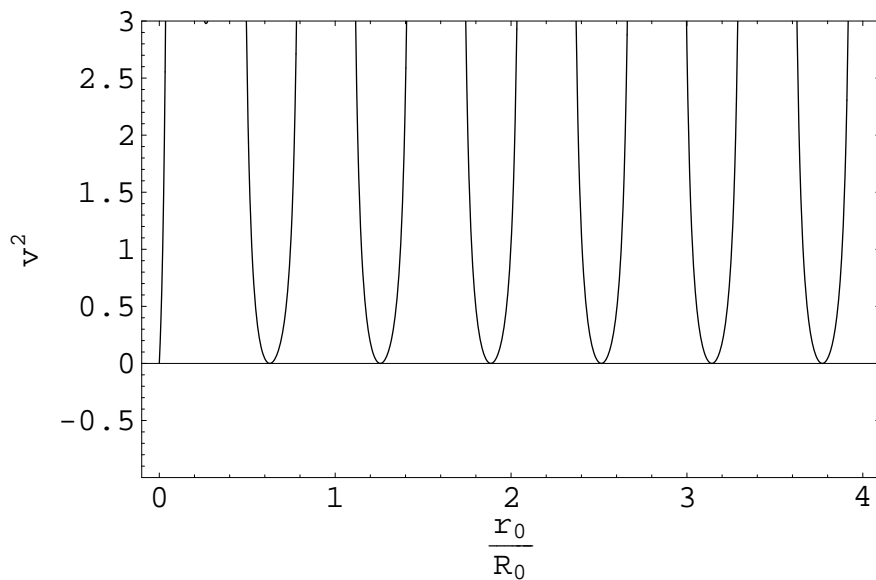


Figure 4.15: The signature $\|v\|^2$ of the trapping horizon formed by the mass distribution $m(r_0) = 0.75 \int_0^{r_0} \sin^2(5x) dx$, which describes concentric infalling shells, is shown here as a function of initial radius r_0 .

We can analyse the situation of multiple infalling shells more closely by considering two successive pulses described by a mass distribution of the form

$$m(r_0) = m_A + m_{B1} \int_0^{r_0} \frac{1}{\sqrt{\pi}} e^{-(x-r_{p1})^2} dx + m_{B2} \int_0^{r_0} \frac{1}{\sqrt{\pi}} e^{-(x-r_{p2})^2} dx \quad (4.5)$$

where m_{Bi} and r_{pi} are the masses and initial radii of the two pulses, respectively. The density and mass profiles for this distribution are shown in Figures 4.16 (a) and (b).

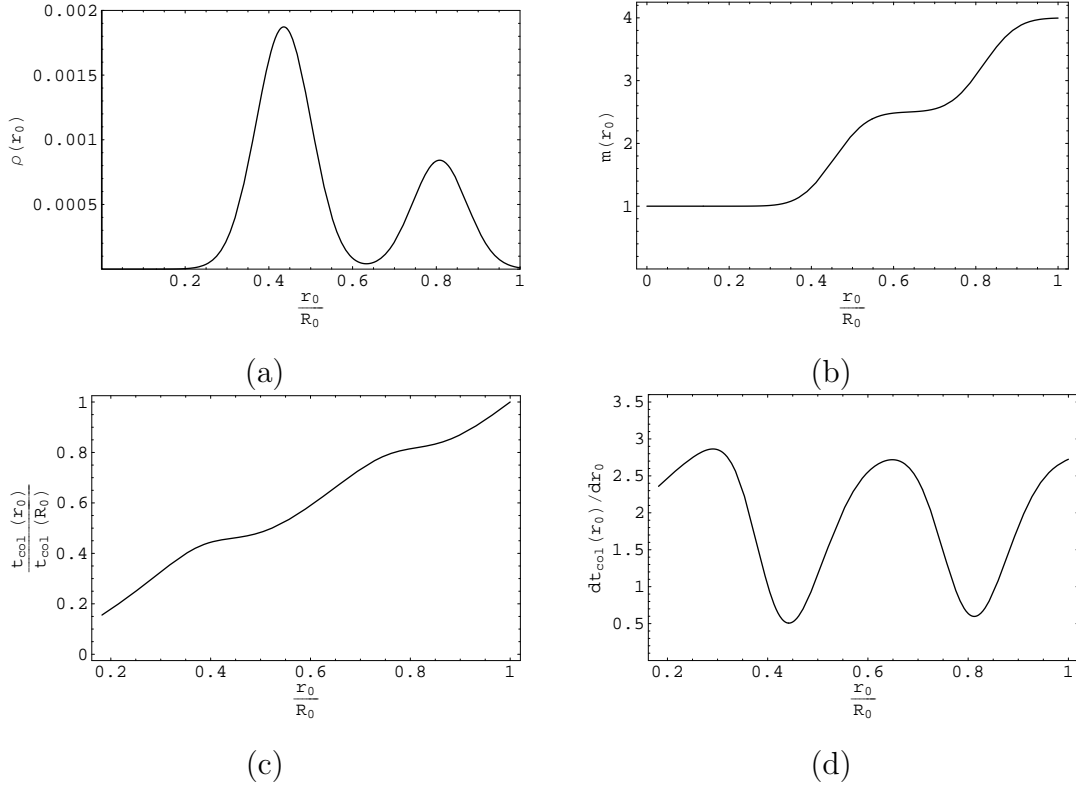


Figure 4.16: The density and mass profiles for the mass distribution given by $m(r_0) = 1 + \int_0^{r_0} \frac{1}{\sqrt{\pi}} e^{-(x-5)^2} dx + 1.5 \int_0^{r_0} \frac{1}{\sqrt{\pi}} e^{-(x-9)^2} dx$ is shown in (a) and (b) respectively, while it is verified that shell crossing does not occur as can be seen in (c) and (d).

Looking at Figure 4.17, we can again see that local increases in density have the effect of pulling the trapping horizon backward through our comoving proper time coordinate. Thus far this has been given only as a descriptive explanation where it has been understood that onset of marginal surface formation is hastened by these increases in density. However, since the shell label and comoving proper time actually form the basis for our coordinate system, and since the trapping horizon is dependent on the geometric properties of the manifold, these two descriptions are essentially equivalent.

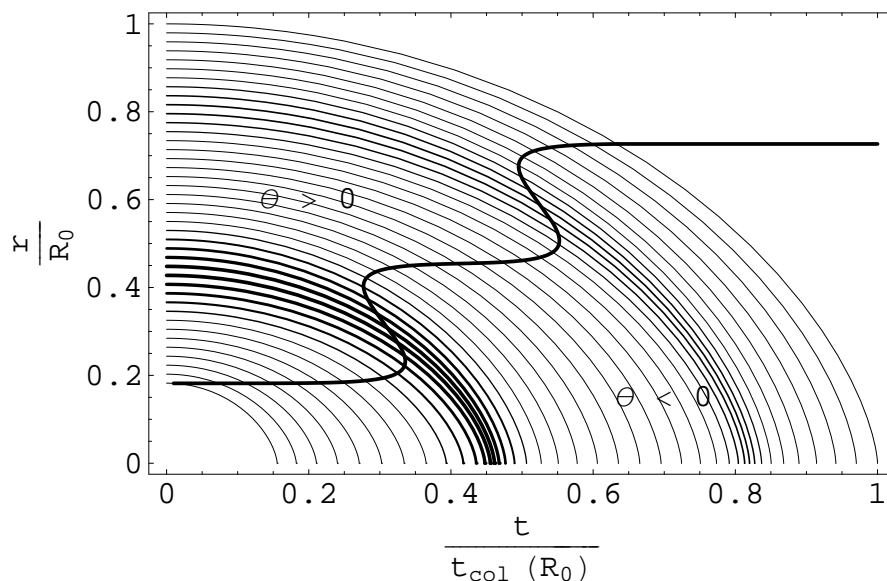


Figure 4.17: Collapse of 40 concentric shells is plotted for the mass distribution given by $m(r_0) = 1 + \int_0^{r_0} \frac{1}{\sqrt{\pi}} e^{-(x-5)^2} dx + 1.5 \int_0^{r_0} \frac{1}{\sqrt{\pi}} e^{-(x-9)^2} dx$. The areal radius of each shell is plotted as a function of comoving proper time. The shells are weighted according to their relative densities as a guide to the eye. The trapping horizon is indicated by the bold curve.

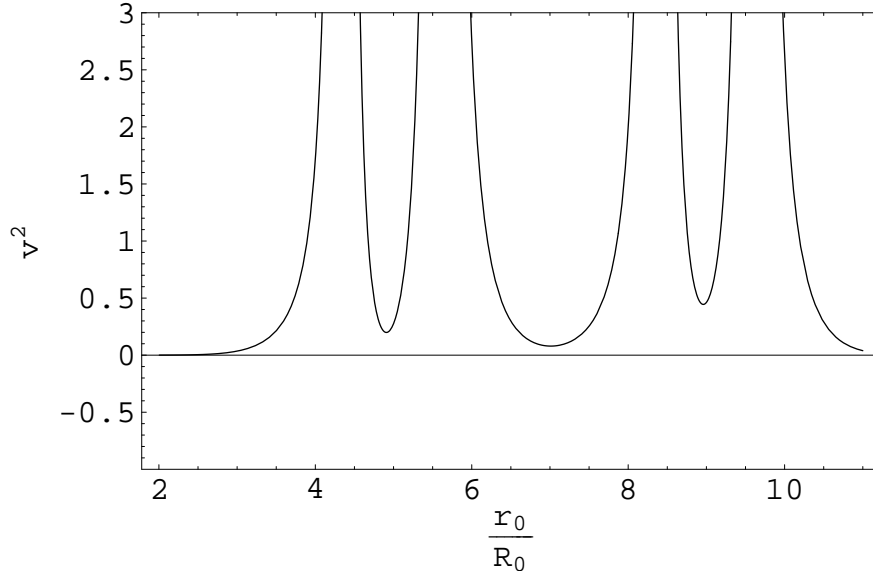


Figure 4.18: The signature $\|v\|^2$ of the trapping horizon formed by the mass distribution $m(r_0) = 1 + \int_0^{r_0} \frac{2}{\sqrt{\pi}} e^{-(x-5)^2} dx$, which describes concentric infalling shells, is shown here as a function of initial radius r_0 .

4.3 Homogeneous Collapse with Initial Velocity

In order to see the effect of non-zero initial velocity on both gravitational collapse and the formation of the trapping horizon, it is prudent to revisit the case of uniform initial density. While we may at first choose a constant initial velocity also, caution is necessary to ensure that the shells move in a timelike manner. For this particular distribution, the divergence of the $\frac{1}{r^2}$ term requires that we make \dot{r}_0 go to zero sufficiently fast towards the coordinate singularity. We can satisfy this by taking

$$\dot{r}_0(r_0) = v_0 \cos\left(\frac{\pi r_0}{2 r_s}\right)^2, \quad (4.6)$$

where v_0 and r_s are suitable scaling parameters. Again, Figures 4.19 (a) and (b) confirm that this distribution does not form shell crossing singularities during its collapse.

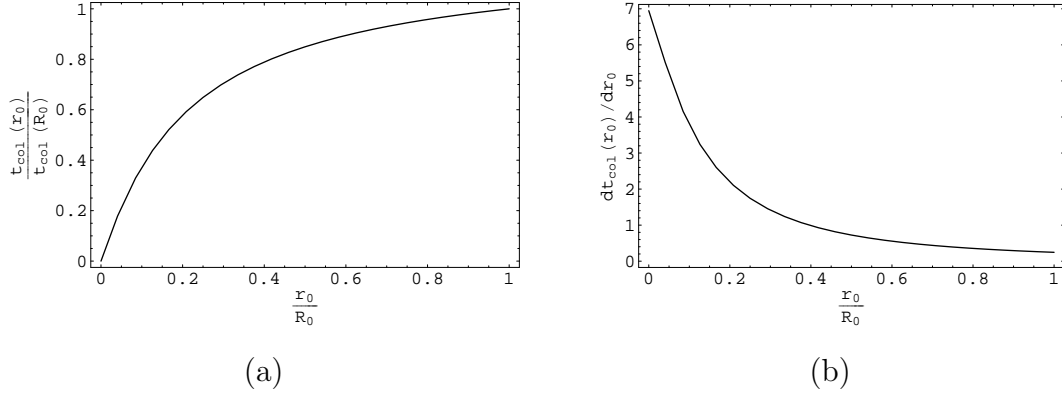


Figure 4.19: The time to collapse, t_{col} , as well as $\frac{dt_{col}}{dr_0}$ are shown for a homogeneous mass distribution with initial velocity profile give by $\dot{r}_0(r_0) = -0.15 \cos\left(\frac{\pi}{2} \frac{r_0}{0.329}\right)^2$.

The collapse for this distribution is shown in Figure 4.20. An interesting distinction from the homogeneous collapse from rest (see Figure 4.1) is that the innermost region becomes trapped at a much earlier time. In fact, in the Oppenheimer Snyder case, this region only becomes trapped on the very boundary of the manifold (at the moment the outermost shell reaches $r = 0$). In each collapse from rest considered thus far where an initial singularity was not present, the innermost shells were essentially in flat, unperturbed space, so that these shells did not form marginal surfaces as quickly as those at greater radii. The effect of imposing a non-zero initial velocity on the collapse is to cause a singularity to form immediately, so that innermost shells become trapped during the beginning of the collapse.

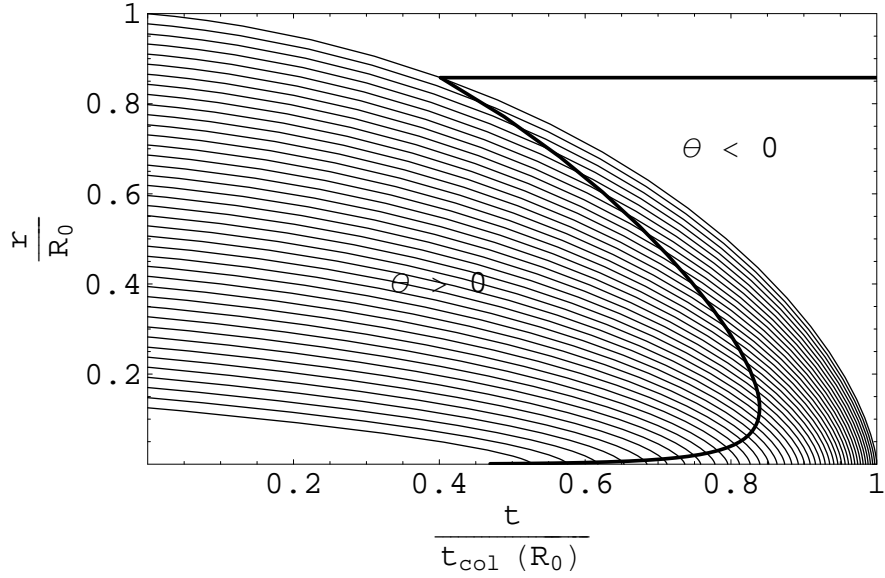


Figure 4.20: Collapse of 20 concentric shells in a homogeneous mass distribution with initial velocity profile give by $\dot{r}_0(r_0) = -0.15\cos\left(\frac{\pi}{2}\frac{r_0}{0.329}\right)^2$ is shown here. The areal radius of each shell is plotted as a function of comoving proper time. $R_0 \approx 0.32$ and $\rho = 1$. The trapping horizon is indicated by the bold curve.

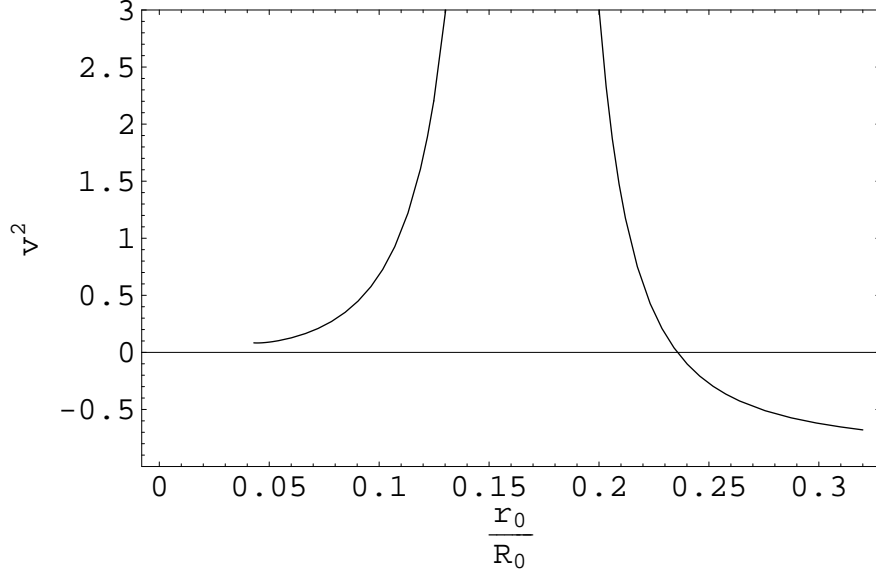


Figure 4.21: The signature $\|v\|^2$ of the trapping horizon formed by a homogeneous mass distribution with initial velocity profile give by $\dot{r}_0(r_0) = -0.15\cos\left(\frac{\pi}{2}\frac{r_0}{0.329}\right)^2$ is shown here as a function of initial radius r_0 .

4.4 General Inhomogeneous Collapse

We also can revisit the case of multiple infalling shells (See Figure 4.14), using a non-zero initial velocity profile. Given a density profile of the form $\rho \sim \sin^2(r_0)$, we can avoid shell crossing by forcing denser regions to move more slowly than sparser ones, while keeping all shells moving in a timelike manner. This can be done by a velocity profile of the form $\dot{r}_0(r_0) = \frac{\cos^2(r_0)}{r_0}$. The time to collapse, t_{col} , as well as $\frac{dt_{col}}{dr_0}$, are shown in Figures 4.22 (a) and (b) for this type of distribution.

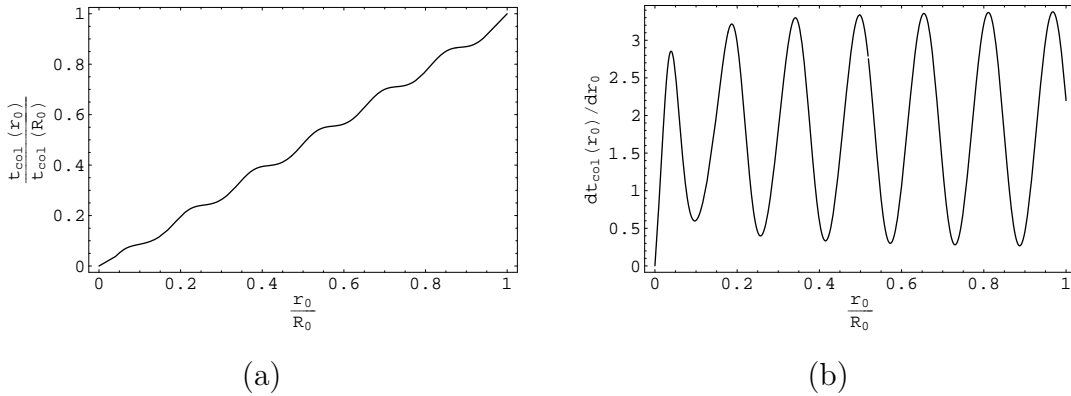


Figure 4.22: The time to collapse, t_{col} , as well as $\frac{dt_{col}}{dr_0}$ are shown for the mass distribution given by $m(r_0) = 0.75 \int_0^{r_0} \sin^2(5x) dx$. Here the initial velocity profile is given by $\dot{r}_0(r_0) = -0.15 \frac{\cos^2(5r_0)}{r_0}$. It is verified that shell crossing does not occur for this distribution.

Figure 4.23 shows the formation of the trapping horizon for this matter system. While it is not fundamentally different from the same density distribution falling from rest, the same trapped region forms near r_0 as in the case of homogeneous collapse with initial velocity, indicating the formation of a singularity early on in the collapse.

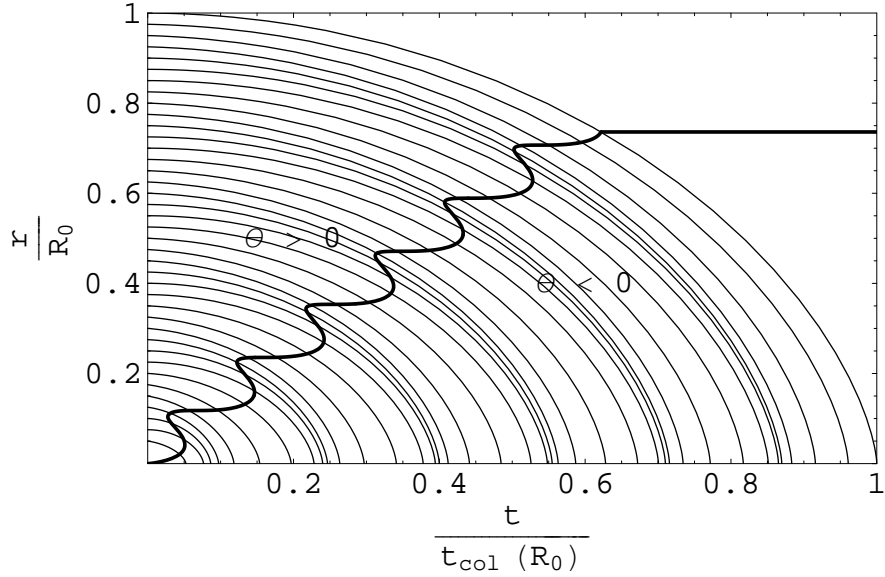


Figure 4.23: Collapse of 40 concentric shells is plotted for the mass distribution given by $m(r_0) = 0.75 \int_0^{r_0} \sin^2(5x) dx$, and the initial velocity profile is given by $\dot{r}_0(r_0) = -0.15 \frac{\cos^2(5r_0)}{r_0}$. The areal radius of each shell is plotted as a function of comoving proper time. The trapping horizon is indicated by the bold curve.

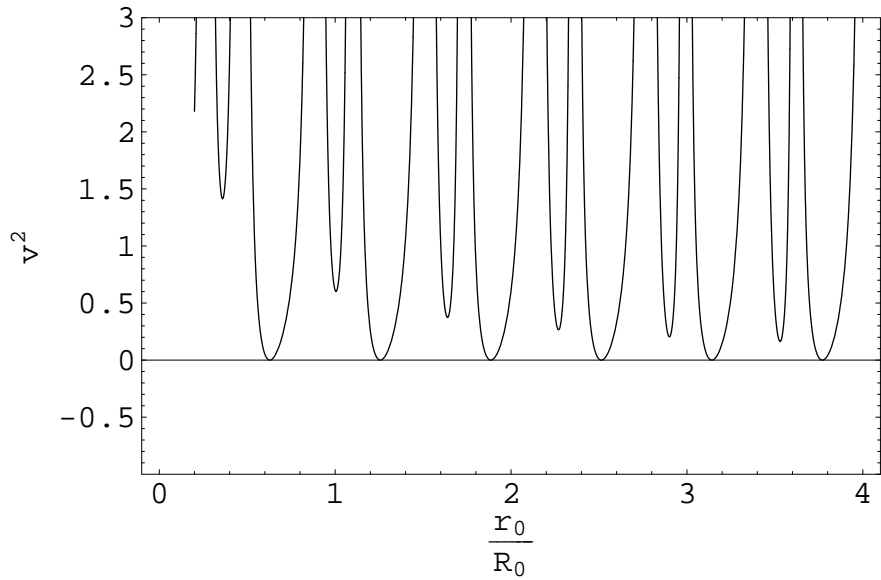


Figure 4.24: The signature s^2 of the trapping horizon formed by the mass distribution $m(r_0) = 0.75 \int_0^{r_0} \sin^2(5x) dx$ is shown here as a function of initial radius r_0 . The initial velocity profile is given by $\dot{r}_0(r_0) = -0.15 \frac{\cos^2(5r_0)}{r_0}$.

4.5 Causal Structure

When examining the signatures of the trapping horizons obtained in the above examples, a difficulty arises with our interpretation of a trapping horizon, or more specifically, a trapped surfaces, which isn't immediately evident from the definition given in Chapter 2. The difficulty arises in situations where the trapping horizon intersects surfaces of constant proper time at multiple points, so that multiple marginal surfaces form (See Figure 4.25). An observer interior to one of these marginal surfaces may nevertheless be in an untrapped region (where $\theta_{(\ell)} > 0$). On the other hand, an observer just outside the marginal surface, who finds himself inside a trapped region (where $\theta_{(\ell)} < 0$) can easily travel through the marginal surface into the untrapped region Booth [2005]. Therefore the notion of a trapped region enclosed by a trapping horizon as a region of no escape is not quite correct, so that the trapping horizon isn't always a horizon in the regular sense. Nevertheless, an observer caught inside the outer marginal surface is constrained to fall into the singularity within a finite lapse of proper time, even though he might move between trapped and untrapped regions from time to time. This is a consequence of the Penrose-Hawking singularity theorem; see for example Penrose [1964].

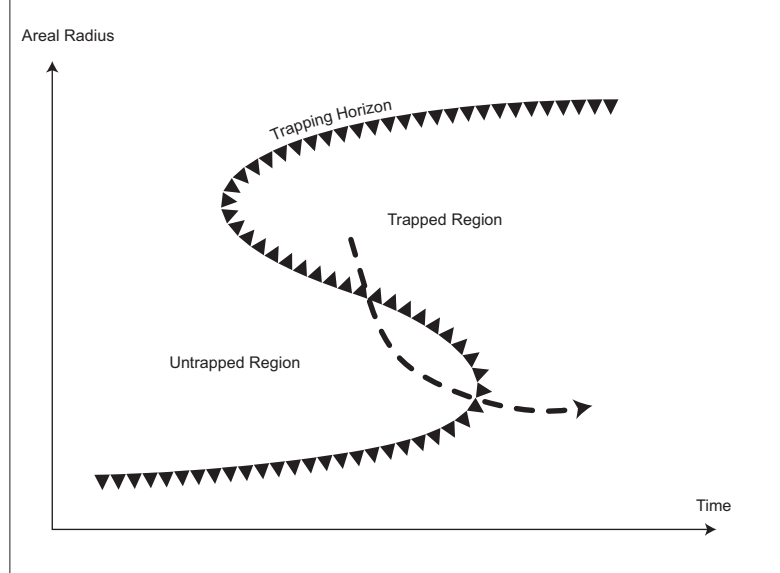


Figure 4.25: An observer inside a trapped region can momentarily escape into the untrapped region before becoming trapped again.

4.6 Horizon Signature

It is important to note that the norms $\|v\|^2$ of tangent vectors on the horizon go to zero as the horizon tends towards equilibrium (i.e., when no matter is falling in); see for example Figures 4.4, 4.7 and 4.18. This is consistent with the requirement that isolated (non-interacting) horizons be null 3-surfaces [Ashtekar, 2000].

In regions where multiple marginal surfaces exist on the same $t = \text{const}$ hypersurface, $\|v\|^2$ changes sign so that the horizon is at times timelike rather than spacelike. This observation is at odds with the common assertion that dynamical horizons are either spacelike or null [Ashtekar and Krishnan, 2003]. To see how this argument arises, we can define a vector field \mathcal{V} that is tangential to the horizon and that is everywhere orthogonal to the foliation by marginal surfaces, which also preserves the foliation, so that $\mathcal{L}_{\mathcal{V}}\theta_{(\ell)} = 0$. Furthermore, we can choose ℓ and n such that $\mathcal{V}^\alpha = \ell^\alpha - Cn^\alpha$ for some scalar field C , which captures the expansion of the horizon. Since $\mathcal{V}^\alpha\mathcal{V}_\alpha = 2C$,

the horizon is either spacelike, timelike or null depending on whether C is positive, negative or zero, respectively. Since $\mathcal{L}_\nu\theta_{(\ell)} = 0$, it follows that

$$\mathcal{L}_\ell\theta_{(\ell)} = C\mathcal{L}_n\theta_{(\ell)}. \quad (4.7)$$

From the null Raychaudhuri's equation, 2.16, it follows that

$$C\mathcal{L}_n\theta_{(\ell)} = -R_{\alpha\beta}\ell^\alpha\ell^\beta, \quad (4.8)$$

where we have used the fact that $\theta_{(\ell)} = 0$ on the horizon, and we have dropped the shear and rotation terms for clarity, since these do not affect the argument. From the null energy condition, which we have assumed to hold, the right hand side of this equation must be negative or zero. Therefore if $\mathcal{L}_n\theta_{(\ell)}$ is taken non-positive, then C must be positive or zero, so that the horizon must be either spacelike or null. See Hayward [1994] for a detailed proof.

In our treatment we have lifted the requirement that $\mathcal{L}_n\theta_{(\ell)} < 0$ in order to study the full richness of the spacetime. The result is that segments of the horizon where the two definitions do not agree are not formed by outermost marginal surfaces, and are not technically horizons in the conventional sense, as was discussed in the previous section. However, these marginal surfaces have quasilocal significance in that they capture the intuitive notion of a region from in which signals are trapped, if only momentarily. For a discussion that attempts to refine this intuitive notion of black hole boundaries in terms of “marginally trapped tubes”, see Booth et al. [2005].

Chapter 5

Conclusion

While first studying single perturbations of the isolated trapping horizon and subsequently the effects of multiple infalling shells on the space-time, we have observed both timelike and spacelike, as well as momentary null evolutions. The point at which a particular shell forms a marginal surface $(r_{TH} = 2m(r_0), t_{TH}(r_0))$ was seen to be related mainly to the density profile in the neighbourhood of that surface, in the sense that the interplay between gravitational and geometrical effects determine the time it takes for a particular shell to reach its particular gravitational radius.

The difficulty in selecting initial conditions that are both physically plausible and well behaved makes the limitations of this model apparent. The occurrence of shell-crossing singularities can only be prevented by choosing appropriately balanced density distributions or by introducing interparticle interaction, i.e., pressure, into the analysis. The latter approach was specifically avoided here because of the problems associated with shock-front formation. While neglecting the effects of pressure limits the physical reach of the model, we gain insight into the dynamics of space-time at considerable economy.

5.1 Future Work

The tractability of the equations of motion that describe inhomogeneous pressure-free collapse suggest possible directions for future study, especially for numerical work. The analysis done here has mainly been concerned with locating trapping horizons and studying their properties, while only passing mention has been made to the event horizon when it could be located unequivocally from the vacuum Schwarzschild solution. It would be interesting to study the relationship between the event horizon and trapping horizons in cases where the dynamic evolution of the event horizon still takes place, i.e., before the two horizons finally merge.

Generally, locating the event horizon is equivalent to determining the causal past of future null infinity, $J^-(\mathcal{I}^+)$, for instance by finding those points in space-time which are able to reach \mathcal{I}^+ through null geodesics. Because of the relative simplifications afforded by spherical symmetry, only maximal (i.e. radially directed) geodesics need to be considered. Therefore, in the case where the entire future of the matter distribution is known, the paths of outgoing light-rays can be solved for, at least numerically, in order to determine whether those paths eventually terminate on \mathcal{I}^+ .

A naïve numerical implementation might conceptually place the dynamic region of the space-time on an adaptive grid which is then surrounded by the vacuum Schwarzschild solution. A geodesic originating from a particular grid point could then be extrapolated towards one of the boundaries of the grid, from where its final fate can be determined.

Appendix A

Detailed Derivations

A.1 Derivation of $\frac{1}{\sqrt{h}}\mathcal{L}_{(\ell)}\sqrt{h} = \theta_{(\ell)}$

Since h is a scalar quantity, we can use the chain rule, so that

$$\mathcal{L}_{\ell}\sqrt{h} = \frac{1}{2\sqrt{h}}\mathcal{L}_{\ell}h. \quad (\text{A.1})$$

Now, Jacobi's classical result for the derivative of a determinant of a matrix $A(\alpha)$ with respect to a parameter α is

$$\frac{d}{d\alpha}\det A(\alpha) = \det A(\alpha)\text{tr}\left(A(\alpha)^{-1}\frac{dA(\alpha)}{d\alpha}\right), \quad (\text{A.2})$$

so that

$$\begin{aligned}
\mathcal{L}_\ell \sqrt{h} &= \frac{1}{2} \sqrt{h} h^{\alpha\beta} \mathcal{L}_\ell h_{\alpha\beta} \\
&= \frac{1}{2} \sqrt{h} h^{\alpha\beta} (\ell^\gamma h_{\alpha\beta;\gamma} + h_{\alpha\gamma} \ell^\gamma_{;\beta} + h_{\gamma\beta} \ell^\gamma_{;\alpha}) \\
&= \frac{1}{2} \sqrt{h} h^{\alpha\beta} (h_{\alpha\gamma} \ell^\gamma_{;\beta} + h_{\gamma\beta} \ell^\gamma_{;\alpha}) \\
&= \sqrt{h} h^{\alpha\beta} h_{\alpha\gamma} \ell^\gamma_{;\beta} \\
&= \sqrt{h} h^{\alpha\beta} \ell_{\alpha;\beta} \\
&= \sqrt{h} \ell^\alpha_{;\alpha} \\
&= \sqrt{h} \theta_{(\ell)},
\end{aligned} \tag{A.3}$$

which completes the derivation.

A.2 Proof that $\tilde{B}_\alpha^\alpha = B_\alpha^\alpha$

$$\begin{aligned}
\tilde{B}_\alpha^\alpha &= g_\alpha^\beta h_\mu^\alpha h_\beta^\nu B_\nu^\mu \\
&= h_\mu^\alpha h_\alpha^\nu B_\nu^\mu \\
&= (g_\mu^\alpha + \ell^\alpha n_\mu + n^\alpha \ell_\mu)(g_\alpha^\nu + \ell^\nu n_\alpha + n^\nu \ell_\alpha) B_\nu^\mu \\
&= (g_\mu^\nu + \ell^\nu n_\mu + n^\nu \ell_\mu + \ell^\nu n_\mu - n_\mu \ell^\nu + n^\nu \ell_\mu - \ell_\mu n^\nu) B_\nu^\mu \\
&= (g_\mu^\nu + n^\nu \ell_\mu + \ell^\nu n_\mu) B_\nu^\mu \\
&= B_\mu^\mu + n^\nu \ell_\mu \ell_{;\nu}^\mu + \ell^\nu n_\mu \ell_{;\nu}^\mu \\
&= B_\mu^\mu + n^\nu \ell_\mu \ell_{;\nu}^\mu \\
&= B_\mu^\mu + \frac{1}{2} n^\nu \ell_\mu \ell_{;\nu}^\mu + \frac{1}{2} n^\nu \ell_\mu \ell_{;\nu}^\mu \\
&= B_\mu^\mu + \frac{1}{2} n^\nu \ell_\mu \ell_{;\nu}^\mu + \frac{1}{2} n^\nu \ell^\mu \ell_{\mu;\nu} \\
&= B_\mu^\mu + \frac{1}{2} n^\nu \ell_{\mu;\nu}^\mu \\
&= B_\mu^\mu
\end{aligned}$$

A.3 Derivation of Equation of Motion

In order to derive equation 2.27 that governs the collapse of the matter distribution, we need to make use of the Einstein field equations, $G_{\alpha\beta} - 8\pi T_{\alpha\beta} = 0$. The stress-energy tensor is of the form,

$$T_{\alpha\beta} = \begin{pmatrix} e^{-2\Phi}\rho & 0 & 0 & 0 \\ 0 & \frac{Pr^2}{\Gamma^2} & 0 & 0 \\ 0 & 0 & Pr^2 & 0 \\ 0 & 0 & 0 & Pr^2 \sin^2 \theta \end{pmatrix}. \quad (\text{A.4})$$

Therefore we have that $G_{ta} = 0$, or that

$$\begin{aligned} \Phi_a r_t &= \frac{r_a \Gamma_t}{\Gamma}, \\ e^{-\Phi} \Phi_a r_t &= e^{-\Phi} \frac{r_a \Gamma_t}{\Gamma}, \\ \Phi' \dot{r} &= \frac{r' \dot{\Gamma}}{\Gamma}. \end{aligned} \quad (\text{A.5})$$

Additionally, we have that $G_{tt} = 8\pi\rho e^{-2\Phi}$, so that

$$\begin{aligned} \frac{1}{r^2} - \frac{\Gamma^2}{r^2} + \frac{e^{-2\Phi} r_t^2}{r^2} - \frac{2\Gamma\Gamma_a}{rr_a} - \frac{2e^{-2\Phi} r_t \Gamma_t}{\Gamma r} + \frac{2e^{-2\Phi} r_t r_{t,a}}{rr_a} &= 8\pi\rho \\ \frac{r'}{2} - \frac{r' \Gamma^2}{2} + \frac{\dot{r}^2 r'}{2} - r\Gamma\Gamma' - \frac{\dot{\Gamma} \dot{r} r r'}{\Gamma} + r \dot{r} e^{-\Phi} r_{a,t} &= 4\pi r^2 r' \rho. \end{aligned}$$

Substituting in equation A.5 we get

$$\begin{aligned}
\frac{r'}{2} - \frac{r'\Gamma^2}{2} + \frac{\dot{r}^2 r'}{2} - r\Gamma\Gamma' - \Phi' \dot{r}^2 r + r\dot{r}e^{-\Phi} r_{a,t} &= 4\pi r^2 r' \rho \\
\frac{r'}{2} - \frac{r'\Gamma^2}{2} + \frac{\dot{r}^2 r'}{2} - r\Gamma\Gamma' + r\dot{r} \left(\frac{\partial \dot{r}}{\partial a} \right) &= 4\pi r^2 r' \rho \\
\frac{\partial}{\partial a} \left(\frac{r}{2} - \frac{r\Gamma^2}{2} + \frac{r\dot{r}^2}{2} \right) &= 4\pi r^2 r' \rho
\end{aligned}$$

Integrating both sides yields the desired result, after some rearrangement,

$$1 - \Gamma^2 + \dot{r}^2 = \frac{2m}{r}. \quad (\text{A.6})$$

Bibliography

- C. W. Misner and D. H. Sharp. Relativistic equations for adiabatic, spherically symmetric gravitational collapse. *Phys. Rev.*, 136:B571, October 1964.
- S. Gonçalves. Shell crossing in generalized Tolman-Bondi spacetimes. *Phys. Rev. D*, 63(12):124017, June 2001.
- J. Bardeen, B. Carter, and S. Hawking. The four laws of black hole mechanics. *Com. Math.*, 31, 1973.
- N. Kimberly. Gravitational waves from gravitational collapse. *Living Reviews in Relativity*, 6, 2003.
- C. Gundlach. Critical phenomena in gravitational collapse. *Living Reviews in Relativity*, 2, 1999.
- M.W. Choptuik. *Deterministic chaos in general relativity, in Deterministic chaos in general relativity*. Plenum Press, New York, 1994.
- S.A. Hayward. General laws of black-hole dynamics. *Phys. Rev. D*, 49:6467–6474, 1994.
- A. Ashtekar and B. Krishnan. Dynamical horizons and their properties. *Phys. Rev. D*, 68:104030, 2003.

- J. Wheeler, K. Thorne, and C. Misner. *Gravitation*. W. H. Freeman, San Francisco, 1973.
- K. Martel and E. Poisson. Regular coordinate systems for schwarzschild and other spherical spacetimes. *Am. J. Phys.*, 69, 2001.
- P.K. Townsend. Black Holes. *ArXiv General Relativity and Quantum Cosmology e-prints*, July 1997.
- S.W. Hawking and G.F.R. Ellis. *The Large Scale Structure of Space-Time*. Cambridge University Press, Cambridge, 1973.
- R.M. Wald. *General Relativity*. The University of Chicago Press, Chicago and London, 1984.
- R. Penrose. Gravitational collapse and space-time singularities. *Phys. Rev. Lett.*, 14: 57, 1964.
- A. Ashtekar. Interface of general relativity, quantum physics and statistical mechanics: Some recent developments. *Ann. Phys.*, 9:178–198, 2000.
- E. Poisson. *A Relativist's Toolkit: The Mathematics of Black-Hole Mechanics*. Cambridge University Press, Cambridge, 2004.
- S.A. Hayward. Black holes: New horizons. *Proceedings of The Ninth Marcel Grossmann Meeting*, 2002.
- M. May and R. White. Hydrodynamic calculations of general-relativistic collapse. *Phys. Rev.*, 141:1232–1241, 1966.
- M. May and R. White. Stellar dynamics and gravitational collapse. *Methods in Computational Physics*, 73:219–258, 1967.

H. Bondi. Spherically symmetrical models in general relativity. *General Relativity and Gravitation*, 31:1783–1805, August 1947.

N. Humphreys, R. Maartens, and D. Matravers. Regular spherical dust spacetimes. *ArXiv General Relativity and Quantum Cosmology e-prints*, April 1998.

T. P. Singh. Null Geodesic Expansion in Spherical Gravitational Collapse. *ArXiv General Relativity and Quantum Cosmology e-prints*, November 1997.

I. Booth. Personal Communication, 2005.

I. Booth, L. Brits, J. Gonzalez, and C. Van Den Broeck. Marginally trapped tubes and dynamical horizons. Not yet published, 2005.

